Office of Naval Research

Contract N5ORI-76 · Task Order No. 1 · NR-071-012

THE DISTRIBUTION OF SPACE CHARGE IN THE HULL MAGNETRON DIODE

By

John A. Bradshaw

August 15, 1954

Technical Report No. 201

Cruft Laboratory
Harvard University
Cambridge, Massachusetts

Office of Naval Research

Contract N5ori-76

Task Order No. 1

NR-071-011

Technical Report

on

The Distribution of Space Charge in the Hull Magnetron Diode

by

John A. Bradshaw

The research reported in this document was made possible through support extended Cruft Laboratory, Harvard University, jointly by the Navy Department (Office of Naval Research), the Signal Corps of the U. S. Army, and the U. S. Air Force, under ONR Contract N5ori-76, T. O. 1.

Technical Report No. 201

Cruft Laboratory

Harvard University

Cambridge, Massachusetts

Table of Contents

TR201

The Distribution of Space Charge in the Hull Magnetron Diode

by

John A. Bradshaw

Cruft Laboratory, Harvard University

Cambridge, Massachusetts

Abstract

If, in a magnetron diode, the current is not limited by cathode temperature, then the radial dependence of the potential and the charge density functions may be found before cutoff from Langmuir's solution, modified by effects of increasing transit time. In the cutoff transition and after cutoff, the cathode temperature, as reflected in the distribution of electronic velocities at emission, affects the potential and density functions. Data on anode current characteristics are compared with calculations based on models that include these temperature effects.

The data from T.R. 185 on probe signal absorption are interpreted as showing that the space-charge cloud extends clear to the anode even after cutoff, and is not bounded by the so-called Hull radius. This and other evidence point to electronic interactions as the source of a mechanism for transporting charge through the cloud from cathode to anode. Finally, the electronic distribution in phase space is stated in a form which could be verified and refined by further experiments.

TR201

The Distribution of Space Charge in the Hull Magnetron Diode

I

Transit Time Effects before Cutoff

a. Introduction

This report supplements Technical Report No. 185, entitled "A Probe Signal Study of the Hull Magnetron Diode." In the following pages we attempt to fit the TEM probe resonance data into a self-consistent model of the magnetron diode. In the fifth and last chapter we present the most controversial aspects of our model of the space charge distribution after cutoff. In the chapters preceding that one we present further data on emission and leakage currents in the experimental diode, and examine in some detail the effects of a thermal distribution of emission velocities on the anode current and on the space charge distribution. In this first chapter we consider the effects of the transit time of electrons in a weak magnetic field.

The Hull cutoff transition in the plate current characteristic of a magnetron diode clearly divides the problem of the radial distribution of space charge within the tube into two sections. Since the main features of these sections and the boundary between them depend chiefly on the ratio p of steady anode potential V_a to the square of the magnetic field imposed on the tube, we may follow the French usage and call these two sections regimes, the regime before cutoff, and the regime after cutoff. We thus reserve the word region for spacial regions within the diode.

The regime before cutoff, which we consider in this chapter, is fairly well understood. At the extreme $p \rightarrow \infty$, we have the Langmuir solution for a diode without magnetic field. If a magnetic field is imposed, and if p decreases to the critical or cutoff value, p_c, the increase in the transit time of individual electrons serves to explain the observed decrease in diode current. The effects of transit time were calculated by Benham and Bethenod for a planar magnetron, and by Allis and Brillouin for a cylindrical one. We develop an integral equation as an alternative and perhaps more convenient way to find the anode current as a function of p in a cylindrical tube.

b. Two Calculations for the Linear Magnetron

In a diode without magnetic field the thermionic electrons move to the anode along practically straight lines. Their paths, it seems, depend little on their emission velocities, and their number, outside the virtual cathode, depends little if at all on the total emission. Imposition of a weak magnetic field, of course, deflects these electrons so that they trace longer curved paths, spend more time in transit, and hit the anode at an oblique angle. The anode current I_a falls slightly, and the reason is briefly this: the virtual cathode supplies just enough current to maintain a complete shield ($E_c=0$) against the anode potential. The longer an electron spends in transit, the longer its charge helps to shield the cathode. Hence if the average transit time τ_d increases, fewer electrons need to be released per unit time to maintain the shield, and I_a consequently falls.

For estimating the transit time and its effects, W. Benham [1] in 1935 published an extension of the Langmuir-Child's equation, which he had worked out for a planar magnetron. Following him, we assume a steady state, so the total current per unit area J_x, across any plane x parallel to the planes of the cathode and anode, $x = 0$ and $x = d$ respectively, is independent of time and of x. The electrons have actually a distribution in velocities given by some density function $f(x,\dot{x})$, so we write J_x and the corresponding charge density $\rho(x)$ as:

$$J_x = e\int_{-\infty}^{\infty} \dot{x}f(x,\dot{x})d\dot{x}\ , \quad \rho(x) = e\int_{-\infty}^{\infty} f(x,\dot{x})d\dot{x}\ , \quad \dot{x} \equiv \frac{dx}{dt}\ . \qquad (1.1)$$

For E_1 the electric field within the diode, we have the following relations, the first by assumption, the second as Poisson's equation, and the third Euler's, with the path parameter $\tau \equiv (t-t_o)$:

$$\frac{\partial E}{\partial t} = 0\ , \quad \frac{\partial E}{\partial x} = \frac{\rho(x)}{\epsilon}\ , \quad \frac{dE}{d\tau} = \frac{\partial E}{\partial x}\frac{dx}{d\tau} \qquad (1.2)\ .$$

Defining a velocity $\dot{\underline{x}}$, an average over the electronic distribution, by

$J_x = \rho(x)\,\dot{\underline{x}}(x)$, we conclude:

$$\text{If } \frac{dx}{d\tau} = \dot{\underline{x}}\text{ , then } \frac{dE}{d\tau} = \frac{J_x}{\epsilon}\text{ , a constant.} \tag{1.3}$$

With equation (1.3), often called Llewellyn's equation, one may integrate the equations of the motion of an average electron in a planar diode. However, this requires the average electron to be typical too, or the deviations from the average to be negligible. For interpenetrating beams of particles, or even for swarms with a wide-spread in random velocities such as make up a virtual cathode, Llewellyn's equation has important limitations. These restrictions are discussed by J. R. Knipp [2, page 135], and apply particularly to the magnetron after cutoff, (Chapter IV).

To continue Benham's method we assume a uniform magnetic field B, directed along the z-axis, and represented by $\omega \equiv eB/m$. The average electron, released from the virtual cathode at $x = 0$ with zero velocity at time t_o, obeys the force equation;

$$x'' + \omega^2 x = \frac{eE}{m} = \frac{eJ}{m\epsilon}\tau \equiv C\tau\ , \quad x'' \equiv \frac{d^2x}{d\tau^2} \tag{1.4}$$

This relation implies $E(x=0) = 0$. Two integrals of it, with the initial conditions $x'(0) = x''(0) = 0$ are:

$$x' = (1 - \cos\theta)\frac{C}{\omega^2}\ , \quad x = (\theta - \sin\theta)\frac{C}{\omega^3}\ , \quad \theta = \omega\tau. \tag{1.5}$$

We call θ the transit angle. If $\phi(x)$ is the potential relative to the virtual cathode, a general first integral of (1.4) is the energy equation:

$$x'^2 + \omega^2 x^2 + \frac{2e\phi}{m} = 0\ , \quad \frac{\partial\phi}{\partial x} \equiv -E(x) \tag{1.6}$$

Substituting from (1.5) in (1.6) for x' and x, evaluated at $x = d$, we find p, the normalized potential at the anode, as a function of the angle of transit to the anode, θ_d. Giving the current density J a similar normalization j, we have:

$$p = \frac{1}{2}\left\{1 + j^2(1 - \cos\theta_d)^2\right\}\ , \quad j = (\theta_d - \sin\theta_d)^{-1} \tag{1.7}$$

Here by definition,

$$p \equiv -\frac{eV_a}{m\omega^2 d^2} \quad , \quad j \equiv \frac{eJ}{m\epsilon\omega^3 d} \quad .$$

With (1.7), one could plot j(p) with θ_d as a parameter. (Brillouin does this [3, page 95] without a reference to Benham.) In Fig. 1-1 we plot instead the ratio R(p):

$$R_{(\text{planar})} \equiv \frac{I_a}{I_L} = \frac{9\,j}{4\sqrt{2}\,p^{3/2}} \tag{1.8}$$

R_p shows how much a small magnetic field reduces the anode current I_a in a planar diode from its Langmuir value I_L. In the limit $\theta_d = 0$, or $p \to \infty$ we have the Langmuir-Childs' law, R = 1. In the limit $\theta = 2\pi$ or $p = p_c$, the electronic orbits just graze the anode and experimental curves of the cutoff transition begin to show the effects of a thermal spread in emission velocities. The value $R(p_c) = 0.717$ (Brillouin, page 98 of [3]) has little significance. In the regime well before cutoff, however, where Benham's assumptions apply, his method gives us a complete picture of the planar magnetron and of the effects of τ_d on the anode current.

One may calculate a relation between p and j without introducing Llewellyn's equation explicitly. Bethenod in 1939 [4] gave a method which we sketch here briefly because it introduces the method we use for a cylindrical magnetron, although his results are less transparent than Benham's. He takes as basic relations the energy equation (1.6), Poisson's equation, and the current relation:

$$\frac{d^2\phi}{dx^2} = -\frac{\rho}{\epsilon} \quad , \quad J_x = \dot{x}\,\rho(x) = \text{constant} \tag{1.9}$$

He regards x rather than τ as the independent variable.

We introduce again normalizing definitions:

$$s \equiv (x/d) \quad , \quad \Phi(s) = \frac{-e\phi}{m\omega^2 d^2} \quad , \quad j \equiv \frac{eJ}{m\epsilon\, d\omega^3} \quad .$$

Then using (1.6), (1.9) and an integration by parts we have:

$$\frac{d^2\Phi}{ds^2} = \frac{j}{\sqrt{2\Phi(s) - s^2}} \ , \text{ or } \ \Phi(s) = j\int_0^s \frac{(s-s^*)\,ds^*}{\sqrt{2\Phi(s^*) - (s^*)^2}} \qquad (1.10)$$

In the formal integration, s^* is the integration variable. The integral form is, for the present, a blind alley.

Bethenod introduces an effective potential, $\chi = \phi + \frac{m\omega^2 x^2}{2e}$, a formula which Twiss [5] and many others have used. Some writers interpret $\chi(x)$ as the potential in a coordinate system moving at the velocity $\dot{y}(x) = \omega x$ in the direction perpendicular to both the B- and the E-fields. The value of this interpretation, and the convenience of the formula is often open to question, but in Bethenod's problem it allows us to complete the integration.

Accordingly, we define f(s) to the fourth power, to avoid fractional exponents:

$$f^4(s) \equiv 2\Phi(s) - s^2 \ , \ \frac{d^2 f^4}{ds^2} = 2\left\{\frac{j}{f^2} - 1\right\} . \qquad (1.11)$$

With initial conditions $f = 0 = df^4/ds$ at $s = 0$, the integrals of (1.11) are:

$$\left(\frac{df^4}{ds}\right)^2 = 8jf^2 - 4f^4 \ , \quad s = 2\int_0^{f(s)} \frac{f^2 df}{\sqrt{2j - f^2}} \qquad (1.12)$$

Writing for convenience, $y \equiv f(2j)^{-1/2}$, we find at $s = 1$:

$$1 = 4j\int_0^{y_d} \frac{y^2 dy}{\sqrt{1 - y^2}} = 2j\left[\sin^{-1} y_d - y_d\sqrt{1 - y_d^2}\right] \qquad (1.13)$$

This is an implicit relation between p and j, since we have $y_d = (2p-1)^{1/4} \cdot (2j)^{-1/2}$. The same expression (1.13) can be obtained from Benham's equations (1.7) after eliminating between them the angle θ_d.

c. <u>An Integral Equation for the Cylindrical Magnetron.</u>

In the cylindrical diode, Llewellyn's equation does not yield integrable relations for the electron's average orbit. To show this we give the radial equations comparable with (1.3) and (1.4):

$$\frac{drE}{d\tau} = \frac{I_a}{2\pi\epsilon h} \; ; \quad r\ddot{r} = -\frac{\omega^2}{4}\left[\frac{P^2}{r^2} - r^2\right] + \frac{eI\tau}{2\pi m\epsilon h} \tag{1.14}$$

Here h is the axial length of the cathode. The uniform magnetic field B lies parallel to the cathode and to the z-axis, and is represented again by $\omega \equiv (eB/m)$. $E(r)$ is the radial electric field, derivable from a potential function $\phi(r)$, I_a is the total radial current, a constant, and P, also a constant, is the normalized form of the canonical angular momentum. If the radius of the cathode is r_c and we introduce the normalization $s \equiv (r/r_c)^2$, then:

$$P \equiv \frac{2s}{\omega}\left(\dot{\theta} + \frac{\omega}{2}\right) \; , \quad (\text{TR}185,\ 1.6) \tag{1.15}$$

If the emission velocities, $\dot{r}$ and $r\dot{\theta}$ at $r = r_c$, are negligible, as we assumed above for the linear magnetron, then $P = 1$.

Allis in 1941 [6, pages 10 to 40] developed a solution of (1.14) by inserting in it a series $(r/r_c) = \sum_0^m a_n \tau^n$, and evaluating the a_n coefficients. Slater comments [7, page 353] that these calculations of Allis "do not seem to be particularly accurate" in the regime before cutoff. The seven points on the curve $R_c(p) = I_a/I_L$, the curve for the cylindrical diode in Fig. 1-1, were therefore calculated by a new method. We devote the rest of this chapter to an outline of it.

The method is based on iteration of an integral equation similar to the integral in (1.10). We assume a potential Φ_L, the normalized Langmuir potential which is correct in a diode without magnetic field. We calculate in such a potential the transit time τ as modified by a small magnetic field. We then calculate the potential perturbed by a modification of the transit time. These two steps will be somewhat obscured by an integration by parts. They could be repeated to improve the potential further.

One could start, we note parenthetically, with a charge free diode in a magnetic field, and the appropriate (logarithmic) potential. One would then treat a small current in this diode as a perturbing influence on the potential. After several iterations one should arrive at the same result: the potential, the current and the transit time adjusted into one self-consistent solution. However, Φ_L is closer than a logarithmic form to the desired potential $\Phi(s)$; an integration over Φ_L should therefore give a closer first-order result.

To find the equation for a cylindrical diode that will correspond to (1.10) for a planar one, we take again, this time in cylindrical coordinates, Poisson's equation, the energy equation, and the current relation:

$$\frac{1}{r}\frac{dr}{dr}\frac{d\phi}{dr} = -\frac{\rho}{\epsilon} \;, \quad \dot{r}^2 + (r\dot{\theta})^2 + \frac{2e\phi}{m} = 0 \;, \quad I_a = 2\pi h r \dot{r} \rho \;. \tag{1.16}$$

We assume the virtual cathode at $r = r_c$, the reference for the potential ϕ, releases electrons with negligible velocities. Then P is indeed one, and (1.15) may be used to eliminate $\dot{\theta}$. We rewrite (1.16) in terms of s and a normalized potential Φ:

$$\frac{d}{ds}\frac{sd\Phi}{ds} = +\frac{e\rho}{4m\omega^2\epsilon_o} \;, \quad \dot{s}^2 + \omega^2(s-1)^2 = 8\omega^2 s\Phi \;, \quad I_a = \pi h \dot{s} \rho r_c^2 \tag{1.17}$$

We find the following definitions convenient throughout this report:

$$\Phi \equiv -\frac{e\phi(r)}{m\omega^2 r_c^2} \,. \quad K(s) \equiv \frac{d\Phi}{d\ln s} = \frac{reE(r)}{2m\omega^2 r_c^2} \;, \quad M \equiv \frac{eI_a}{4\pi h m\omega^3 \epsilon_o r_c^2} \tag{1.18}$$

Here K we regard as the normalized electric field and M as the normalized radial current, a constant. If the electric field at the cathode vanishes, $K(r_c) = 0$, and the equations like (1.10) are:

$$\frac{d}{ds}\, s\frac{d\Phi}{ds} = \frac{M}{\sqrt{8s\Phi - (s-1)^2}} \,, \quad \text{or} \quad \Phi(s) = M\int_1^s \frac{(\ln s - \ln s^*)\,ds^*}{\sqrt{8s^*\Phi(s^*) - (s^*-1)^2}} \tag{1.19}$$

Since we propose to build our iterated solution from the well known Langmuir solution, we must write Langmuir's solution in these symbols. If the magnetic field vanishes, Φ proves inconvenient, so for two paragraphs we drop this normalization and write $\psi \equiv -e\phi/mr_c^2 = \omega^2\Phi$. Then, after multiplying the first equation in (1.19) by 4s, we find:

$$\frac{d^2\psi}{d\xi^2} = \frac{eI_a}{2\sqrt{2}\pi h r_c^2 \epsilon m}\;\frac{\exp\xi}{\sqrt{\psi - \frac{\omega^2}{8s}(s-1)^2}} \;, \quad \xi = \frac{1}{2}\ln s \tag{1.20}$$

In (1.20) we may set $\omega^2 = 0$. Then, writing $\psi = k f_L^{4/3}$, we split (1.20) into two relations, one which normalizes f_L and one which gives f_L as a function of ξ:

$$k^{3/2} \equiv \frac{9 e I_a}{8\sqrt{2}\,\pi \epsilon h r_c^2 m} \quad , \quad (f'_L)^2 + 3 f_L f''_L = \exp \xi \quad . \tag{1.21}$$

Langmuir and Mott-Smith [8] developed f_L in a MacLaurin series in ξ from the equation in (1.21) for $f(\xi)$, and from derivatives of this equation, all evaluated at the cathode where $\xi = 0$. For instance $\psi(0) = 0 = f(0)$, and $f'_L(0) = 1$ from (1.21). We find from the first derivative of (1.21):

$$5 f'_L f''_L + 3 f_L f'''_L = \exp(\xi) \quad , \quad \therefore \quad f''_L(0) = \frac{1}{5} \quad . \tag{1.22}$$

This process continues to yield one coefficient per derivative, and the resulting series is:

$$f_L = \xi + \frac{\xi^2}{10} + \frac{\xi^3}{60} + \frac{2\xi^4}{825} + \ldots \equiv \exp(\xi/2) \cdot \beta(\xi) \tag{1.23}$$

$\beta(\xi)$ is the function usually quoted as Langmuir's, rather than f_L, and Langmuir showed that β approaches one as ξ tends to infinity. The series for β is [9]:

$$\beta \equiv \xi - \frac{2}{5}\xi^2 + \frac{11\xi^3}{120} - \frac{47\xi^4}{3300} \ldots \tag{1.24}$$

From (1.20) with $\omega^2 = 0$, we conclude that the equations which f_L satisfies can be written in terms of s as follows:

$$\frac{d}{ds}\, s\, \frac{d f_L^{4/3}}{ds} = \frac{1}{9\sqrt{s f_L^{4/3}}} \quad , \text{ or } \quad f_L(s)^{4/3} = \frac{1}{9}\int_1^s \frac{(\ln s - \ln s^*)\, ds^*}{\sqrt{s^* f_L^{4/3}(s^*)}} \tag{1.25}$$

From (1.23) we conclude that the solution of these is:

$$f_L = \frac{\ln s}{2}\left\{1 + \frac{\ln s}{20} + \frac{(\ln s)^2}{240} + \frac{(\ln s)^3}{3300} + \ldots\right\} = s^{1/4} \cdot \beta(s) \tag{1.26}$$

We also define the first iteration f, over f_L in the presence of a small magnetic field, by comparison of (1.25) with (1.19):

$$f^{4/3}(s) \equiv \frac{1}{9}\int_1^s \frac{(\ln s - \ln s*)\,ds}{\sqrt{s*f_L^{4/3}(s*) - S(s_b, s*)}} \quad . \tag{1.27}$$

When we have found the function S in (1.27) and brought the current density, M in (1.19) or $k^{3/2}$ in (1.21), into the iterated solution, the formulation will be complete.

Now the expression under the square root in the denominator of each integral, (1.19), (1.20), (1.25) or (1.27), represents the radial velocity $\dot{s}^2$ (1.17). In T.R. 185 (1.5) we defined for orbits in a strong magnetic field a turning radius s_b, where $\dot{s}$ vanishes. In the regime before cutoff, the average electron hits the anode before reversing its radial velocity, but we may imagine its path, and the potential $f_L(s)$, extended beyond the anode through the interval $s_a < s < s_b$. Now S represents the effects of a small magnetic field on $\dot{s}$, so from (1.17) S must be proportional to $(s-1)^2$, and S in (1.27) must cause the denominator of the integral to vanish at s_b:

$$S(s, s_b) = \frac{(s-1)^2}{(s_b-1)^2}\, s_b \cdot f_L^{4/3}(s_b) . \tag{1.28}$$

As a check on formula (1.28), we note that S approaches zero like $s_b^{-2/3}$, as s_b approaches infinity with s fixed. As s_b approaches infinity, the magnetic field tends to zero and $f_L(s_b)$ behaves like $s_b^{1/4}$(1.26).

For the first iteration in (1.19) we define the Langmuir trial potential Φ_L by arguments like those for S:

$$\Phi_L(s) = \Phi_b\, f_L^{4/3}(s) \cdot f_L^{-4/3}(s_b) , \quad \Phi_b \equiv (s_b-1)^2 (8 s_b)^{-1} \tag{1.29}$$

This $\Phi_L(s)$ causes the denominator in (1.19) to vanish at s_b. The first iteration from (1.19), with $\Phi(s*) = \Phi_L$ and (1.27) yields:

$$\Phi(s) = M \cdot 9 f^{4/3}(s) \cdot f_L^{2/3}(s_b) \cdot (8\Phi_b)^{-1/2} \tag{1.30}$$

But if $\Phi(s)$ is to be used for another iteration, it must have the same form as $\Phi_L(s)$. Hence:

$$\Phi(s) = \Phi_b\, f^{4/3}(s)\, f^{-4/3}(s_b)\ ,\quad p \equiv \Phi(s_a)\quad . \tag{1.31}$$

$$\therefore\quad M = \Phi_b^{\ 3/2}\, f^{-4/3}(s_b)\, f_L^{-2/3}(s_b)\,(2\sqrt{2}/9) \tag{1.32}$$

With a little more algebra one can find the quantity R_c, plotted on the right in Fig. 1-1:

$$R_c \equiv \frac{I_a}{I_L} = \frac{f_L^2(s_a)}{f^2(s_a)} = \frac{9M}{2\sqrt{2}}\cdot\frac{f_L^2(s_a)}{p^{3/2}}\cdot\frac{f_L^{\ 2/3}(s_b)}{f^{2/3}(s_b)} \tag{1.33}$$

The ratio $\left\{f(s_b)/f_L(s_b)\right\}^{4/3}$ has the value 1.19, found by numerical work to be independent of s_b in the range $7\ 1/4 \leq s_b \leq 29\ 1/4$. The corresponding transit angle $\theta_a(s_b)$ is given by an integral which, like (1.27), can be evaluated numerically, once s_b and s_a are given:

$$\theta_a(s_b) = \int_1^{s_a} \frac{ds}{\sqrt{8s\Phi_L - (s-1)^2}} = \sqrt{\frac{f_L^{\ 4/3}(s_b)}{8\Phi_b}}\int_1^{s_a} \frac{ds}{\sqrt{s\, f_L^{\ 4/3}(s) - S(s,s_b)}}\ . \tag{1.34}$$

This angle appears in the parameter $\overline{m} \equiv 6\,\theta_a/\pi$ along the curve R_c in Fig. 3-1.

This completes our analysis of transit time effects. We delay the presentation of data on the ratio I_a/I_L to Chapter III, where we consider the effects of emission velocities on this ratio. If one holds V_a fixed and increases ω, then as p falls toward the cutoff transition value p_c, the circumferential component of the emission velocity begins to affect the path and transit time of the individual particle. In the cutoff transition the sign of this component practically determines whether the particle reaches the anode or returns to the cathode. For p somewhat larger than p_c, however, the data support the analysis leading to Fig. 1-1, and the conclusion that transit time effects are the chief cause of the observed decrease in I_a accompanying an increase in ω.

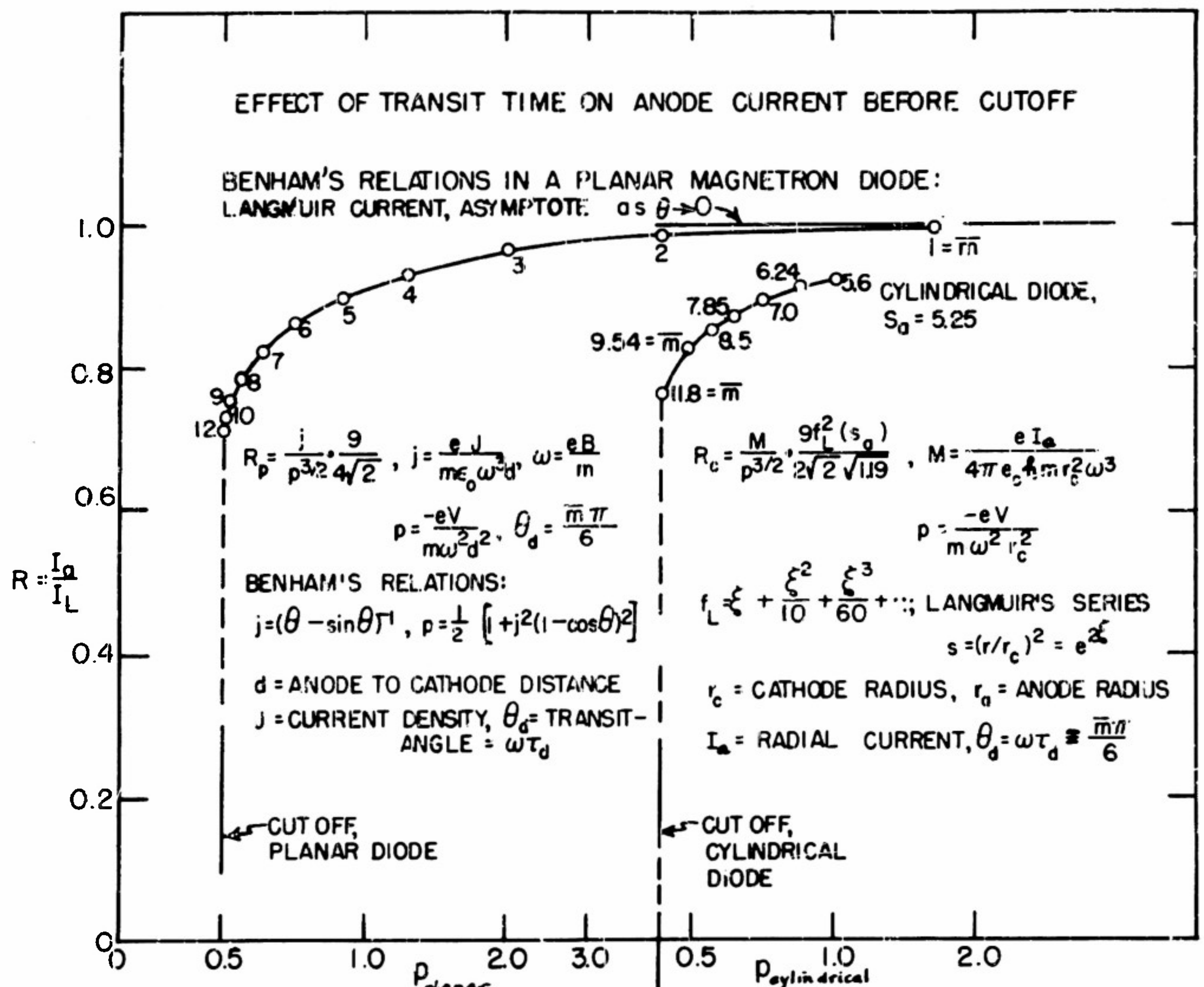
EFFECT OF TRANSIT TIME ON ANODE CURRENT BEFORE CUTOFF
BENHAM'S RELATIONS IN A PLANAR MAGNETRON DIODE:
LANGMUIR CURRENT, ASYMPTOTE as $\theta \to 0$
CYLINDRICAL DIODE, $S_a = 5.25$
$R_p = \frac{j}{p^{3/2}} \cdot \frac{9}{4\sqrt{2}}$, $j = \frac{eJ}{m\epsilon_0 \omega^3 d}$, $\omega = \frac{eB}{m}$
$p = \frac{-eV}{m\omega^2 d^2}$, $\theta_d = \frac{\overline{m}\pi}{6}$
BENHAM'S RELATIONS:
$j = (\theta - \sin\theta)^{-1}$, $p = \frac{1}{2}\left[1 + j^2(1-\cos\theta)^2\right]$
d = ANODE TO CATHODE DISTANCE
J = CURRENT DENSITY, θ_d = TRANSIT-ANGLE = $\omega\tau_d$
$R_c = \frac{M}{p^{3/2}} \cdot \frac{9 f_L^2(s_a)}{2\sqrt{2}\sqrt{1.19}}$, $M = \frac{e I_a}{4\pi \epsilon_0 m r_c^2 \omega^3}$
$p = \frac{-eV}{m\omega^2 r_c^2}$
$f_L = \xi + \frac{\xi^2}{10} + \frac{\xi^3}{60} + \cdots$; LANGMUIR'S SERIES
$s = (r/r_c)^2 = e^{2\xi}$
r_c = CATHODE RADIUS, r_a = ANODE RADIUS
I_a = RADIAL CURRENT, $\theta_d = \omega\tau_d = \frac{\overline{m}\pi}{6}$
CUT OFF, PLANAR DIODE
CUT OFF, CYLINDRICAL DIODE
$R = \frac{I_a}{I_L}$
p_{planar}
$p_{cylindrical}$

FIGURE I-1

References in Chapter I

1. W. E. Benham, "Electronic Theory and the Magnetron Oscillator," Proc. Phys. Soc., London 47 1-53 (1935).

2. Hamilton, Knipp, and Kuper, Klystrons and Microwave Triodes, McGraw-Hill, New York, 1948, Vol. 7 of Rad. Lab. Series.

3. L. Brillouin, "Electronic Theory in the Plane Magnetron," in Advances in Electronics III, L. Marton, Editor, Academic Press, New York, 1951.

4. J. Bethenod, "On the Variation of the Convection Current in a Magnetron under the Action of a Magnetic Field," C.R. Acad. Sci. Paris, 209 832 (1939).

5. R.Q. Twiss, "On the Steady State Theory of the Magnetron," in Advances in Electronics V, L. Marton, Editor, Academic Press, New York, 1953.

6. W. Allis, Theory of the Magnetron Oscillator, Special Report 9S, V, Radiation Laboratory, Cambridge, Massachusetts, 1941.

7. J.C. Slater, Microwave Electronics, Van Nostrand Co., Inc., New York, 1950.

8. Langmuir and Blodgett, "Currents Limited by Space Charge between Coaxial Cylinders," Phys. Rev. 22, 347-356 (1923).

9. I. Langmuir, "The Effect of Space Charge and Residual Gases on Thermionic Currents in High Vacuum," Phys. Rev. 2, 450-486 (1913).

II

Effects of Emission Temperature in a Diode without Magnetic Field

a. Introduction

In this chapter, by a review of the characteristics of a virtual cathode without magnetic field, and by an analysis of experimental data on the emission current I_o, we prepare the way for Chapter III, where we will consider the effects of a magnetic field on the virtual cathode, and the effects of emission temperature on the cutoff transition in the magnetron diode.

The problem of describing space charge in front of an emitting surface is at least forty years old. In 1914 W. Schottky [1] published an analysis of current flowing from an emitting wire to a concentric cylindrical anode against a retarding potential. He found a Maxwellian distribution of emission velocities. In another important paper in 1923, I. Langmuir [2] reviewed a series of calculations on the formation of a virtual cathode, and published tables applicable to a planar diode.

In 1940 E. Wheatcroft [3] gave the results of a unified group of calculations for the position and depth of the potential minimum in front of a cylindrical emitting surface. However, his graphs do not include results applicable to a tube with a large cathode. We have, therefore, used his analysis in somewhat revised form to extend the range of these results so as to apply them to our diode. This revision, outlined below, proves adequate to treat the more general case of the diode in a magnetic field, so it forms the basis of the next chapter as well.

b. Space Charge Inside the Virtual Cathode.

We assume the conventional polar coordinate system ($r\theta z$); the z-axis lies along the center of the set of two coaxial conducting cylinders that constitute the cathode and anode of our diode. Our reference is the emitting surface on the cathode at the radius $r = r_c$. The potential function $\phi(r)$ is zero there, and for $r > r_c$, ϕ is determined by the anode voltage, and the charge distribution which we wish to calculate. We assume in this chapter that electrons suffer neither collisions nor individual interactions, indeed, that the orbits after emission are determined entirely by the emission velocities and by ϕ, through the energy and momentum relations:

$$\frac{mv^2}{2} + e\phi = \frac{mv_c^2}{2} \quad , \quad r^2\dot{\theta} = (r^2\dot{\theta})_c \tag{2.1}$$

We will re-examine these assumptions in Chapter IV.

We now normalize equations (2.1) by dividing them by kT, where k is Boltzmann's constant, and T is the cathode temperature in degrees Kelvin. We also adopt the definitions:

$$s \equiv \left(\frac{r}{r_c}\right)^2 , \quad \psi \equiv \frac{e\phi}{kT} , \quad \bar{x} \equiv \dot{r}\left(\frac{m}{2kT}\right)^{1/2} , \quad \bar{y} \equiv r\dot{\theta}\left(\frac{m}{2kT}\right)^{1/2} . \tag{2.2}$$

Thus $\bar{x}$ and $\bar{y}$ are normalized velocities at some $r > r_c$, while the normalized emission velocities we write without bars. The coordinate z is suppressed, for we assume that ϕ and $\dot{z}$ are independent of z and of time. Equations (2.1) become:

$$\bar{x}^2 + \bar{y}^2 + \psi = x^2 + y^2 , \quad \sqrt{s}\,\bar{y} = y . \tag{2.3}$$

If the distribution of velocities among electrons on emission is Maxweilian, then at the cathode the increment to the normalized charge density dS in any increment dx dy of the plane of emission velocities (x,y) is:

$$dS = \frac{1}{\pi} \exp\left\{-(x^2+y^2)\right\} dx\, dy \tag{2.4}$$

The normalization here is such that the integral $S(r_c)$ over the whole (x,y)-plane is equal to one. If I_o is the emission current, the increment to the total current in the outward radial direction is similarly:

$$dI(r_c) = \frac{2I_o}{\sqrt{\pi}} \exp\left\{-(x^2+y^2)\right\} x\, dx\, dy . \tag{2.5}$$

The integral of dI over the half plane $x > 0$ is just I_o. Under our assumptions, each increment dI is prevented from exchanging electrons with other increments, so as dI moves away from the cathode, it is conserved: $\frac{d(dI)}{dr} \equiv 0$. We wish next to determine how the corresponding charge increment, dS(r), changes as r increases.

To examine the movement of charge away from the cathode, we change to coordinates $(\bar{x}, \bar{y})$ at some fixed radius s. From (2.3) we have the relations:

$$d(\bar{x}^2) + 2\bar{y}\, d\bar{y} = d(x^2) + 2y\, dy , \quad \sqrt{s}\, d\bar{y} = dy . \tag{2.6}$$

The Jacobian of a transformation from (x^2, y) to $(\bar{x}^2, \bar{y})$ is:

$$J = \begin{vmatrix} \dfrac{\partial(x^2)}{\partial(\bar{x}^2)} & \dfrac{\partial(x^2)}{\partial \bar{y}} \\ \dfrac{\partial y}{\partial(\bar{x}^2)} & \dfrac{\partial y}{\partial \bar{y}} \end{vmatrix} = \begin{vmatrix} 1 & f(\bar{x},s) \\ 0 & \sqrt{s} \end{vmatrix} = \sqrt{s} \quad . \tag{2.7}$$

$$\therefore \quad d(x^2)\, dy = \sqrt{s}\; d(\bar{x}^2)\, d\bar{y} \quad . \tag{2.8}$$

Now by (2.3) and (2.8) $dI(r)$ equals $dI(r_c)$ if we have:

$$dI(r) = 2\, I_o \sqrt{\frac{s}{\pi}} \exp\left\{-(\bar{x}^2+\bar{y}^2+\psi)\right\} \bar{x}\, d\bar{x}\, d\bar{y} \quad . \tag{2.9}$$

With a little algebra we obtain the relation of $dI(r)$ to $dS(r)$:

$$dI(r) = 2I_o \sqrt{s\pi}\; \bar{x}\, dS(r) \quad . \tag{2.10}$$

In the limit $r = r_c$ this relation satisfies (2.4) and (2.5). If we write the unnormalized increment of charge density in dS as $d\rho$, then (2.10) represents the relations:

$$dI = 2\pi h r \dot{r}\, d\rho \quad , \quad d\rho = \frac{I_o}{\pi h r_c} \cdot \sqrt{\frac{m\pi}{2kT}}\, dS \quad . \tag{2.11}$$

Equation (2.10) implies the result for $dS(r)$:

$$dS(r) = \frac{1}{\pi} \exp\left\{-(\bar{x}^2+\bar{y}^2+\psi)\right\} d\bar{x}\, d\bar{y} \quad . \tag{2.12}$$

The charge density, normalized with respect to the density at the cathode, is then an integral, $S(r) = \iint dS(r,\bar{x}\bar{y})$ over a region of the $(\bar{x},\bar{y})$-plane. We call this region W and proceed to determine its boundaries: If an electron in its orbit away from the cathode reaches a radius r and thus contributes to $S(r)$, its radial velocity must be positive from r_c all the radial interval to r; in symbols, we require $\bar{x}(r) > 0$, $r \geq r_c$. Secondly, if its total velocity is insufficient to carry it over the maximum of ψ, ψ_m (which is the minimum of $\phi(r)$, since $\underline{e}$ is negative) at the virtual cathode, the electron reverses its radial motion and falls back to the cathode surface. It then contributes twice to $S(r)$, $r < r_m$. These two observations, together with equations (2.3), serve to fix the boundaries of W.

The region of W which represents electrons falling back toward the cathode lies properly in the lower half of the $(\bar{x},\bar{y})$-plane. Since the distribution function $\exp\left\{-(\bar{x}^2+\bar{y}^2+\psi)\right\}$ is symmetric in $\bar{x}$, we may reflect this region about the $\bar{y}$-axis into the upper half of the $(\bar{x}\bar{y})$-plane. We then count cells $d|\bar{x}|dy$ within the reflection twice. Other cells in the upper half plane count once and represent electrons which reach the anode. Still other cells lie outside W, and are empty. These cells lie in a kind of shadow cast by equations (2. 3) on the wings of the $(\bar{x}\bar{y})$-plane.

The virtual cathode lies, of course, at the radius r_m where $d\psi/ds$ is zero. The three sections in Fig. 2-1 represent W for three choices of radius r(or s): $s_m > s > 1$, $s = s_m$ and $s > s_m$. We now undertake a more detailed discussion of the first sketch in order to evaluate S(r).

In Fig. 2-1a, W is bounded near the origin of the $(\bar{x},\bar{y})$-plane by the $\bar{y}$-axis, and in the wings beyond $\bar{y}_3$ by dashed curves, segments of hyperbolae. The hyperbolae intersect the $\bar{y}$-axis at $\bar{y}_1$ and have the equations:

$$x = 0\ ,\quad \bar{x}^2 + \psi = (s-1)\bar{y}^2\ ;\quad \bar{y}_1 \equiv \pm\sqrt{\frac{\psi}{s-1}}\ . \tag{2.13}$$

The dashed elliptic segment $\underline{m}$ represents particles which just reach the virtual cathode, and the region under it includes most of the cells which count twice in the integral S(r). The segment intersects the $\bar{y}$-axis at $\bar{y}_4$ and has the equations:

$$\bar{x}_m = 0\ ,\quad \bar{x}^2 + (1-\frac{s}{s_m})\bar{y}^2 = \psi_m - \psi\ ;\quad \bar{y}_4 \equiv \pm\sqrt{\frac{s_m(\psi_m-\psi)}{s_m-s}} \tag{2.14}$$

The dashed curves and equations (2. 13) and (2. 14) represent roughly the two observations made above on the boundaries of W. We note that the distribution function $\exp\left\{-(\bar{x}^2+\bar{y}^2+\psi)\right\}$ is bell-shaped and centered at the origin of the $(\bar{x},\bar{y})$-plane. It falls off rapidly away from the origin, so the part of W under the curve $\underline{m}$ in Fig. 2-1a is the most important. The excluded wings of the $(\bar{x}\bar{y})$-plane represent very small values of $\exp\left\{-(\bar{x}^2+\bar{y}^2)\right\}$, and S(r) retains a value near $\exp(-\psi)$ as long as $|\bar{y}_4|$ is larger than one.

The true boundaries of W and of the region of double cells are not the dashed curves between points $\bar{y}_3$ and $\bar{y}_1$, $\bar{y}_4$ and $\bar{x}_2$, but the solid lines running diagonally up from $\bar{y}_2$. To explain the solid lines we introduce the notion of an operator P(s) which can transform the plane of emission velocities into the plane $(\bar{x},\bar{y})$ of velocities at the radius s: $(\bar{x},\bar{y}) = P(s)(x,y)$. Under action of P(s), we have seen, the y-axis on the (x,y)-plane maps into the hyperbolic segments (2.13) ending on the $(\bar{x},\bar{y})$-plane at $\bar{y}_1$. P(s) is thus an abbreviation for equations (2.3).

We consider also an inverse mapping $P^{-1}(s*)(\bar{x},\bar{y}) = (x,y)$, which carries features of an $(\bar{x},\bar{y})$-plane, at a radius that we distinguish from s with a star, back on the (x,y)-plane. In particular the $\bar{y}$-axis maps under $P^{-1}(s*)$ into an elliptic segment with the equations ($\psi > 0$):

$$\bar{x} = 0\ , \quad x^2 + y^2\left(1 - \frac{1}{s*}\right) = \psi(s*) \quad ; \quad y_1 \equiv \pm\sqrt{\frac{s*\psi}{s*-1}} \quad . \tag{2.15}$$

For a series of values of s* less than s_m, $P^{-1}(s*)$ represents the condition $\bar{x}(s*) = 0$ by a family of elliptic segments with a smooth envelope that extends on the (x,y)-plane from $y_3 \equiv \pm\sqrt{d\psi/ds}\,\Big|_{s=1}$, x = 0, to y = 0, $x_m \equiv \sqrt{\psi_m}$. The cells dy dx lying outside this envelope represent electrons which will cross r_m and reach the anode. The electrons whose emission velocities lie inside this envelope will return to the cathode. The direct mapping P(s) of this envelope on the $(\bar{x}\bar{y})$-plane in Fig. 2-1a yields the solid lines through $\bar{y}_2$. The points $\bar{y}_2$ represent points y_2 where the particular ellipse for s = s* touches the envelope. The points $\bar{y}_3$ are equal to $y_3/\sqrt{s}$.

Since the mapping P is a continuous function of s, each point (x,y) traces a curve through a succession of $(\bar{x},\bar{y})$-planes. The vector $\underline{t}$ tangent to such a curve can be defined almost everywhere on the $(\bar{x},\bar{y})$-plane with equations (2.3). Introducing unit vectors $\hat{x}$ and $\hat{y}$ along the $\bar{x}$- and $\bar{y}$-axes, and partial derivatives to imply that x and y are held fixed, we write $\underline{t}$:

$$\underline{t} \equiv \hat{x}\frac{\partial\bar{x}}{\partial s} + \hat{y}\frac{\partial\bar{y}}{\partial s} = \hat{x}\left[\frac{\bar{y}^2}{2s\bar{x}} - \frac{1}{2\bar{x}}\frac{d\psi}{ds}\right] - \hat{y}\frac{\bar{y}}{2s} \quad . \tag{2.16}$$

Then the intersection $\bar{y}_2$ is defined thus:

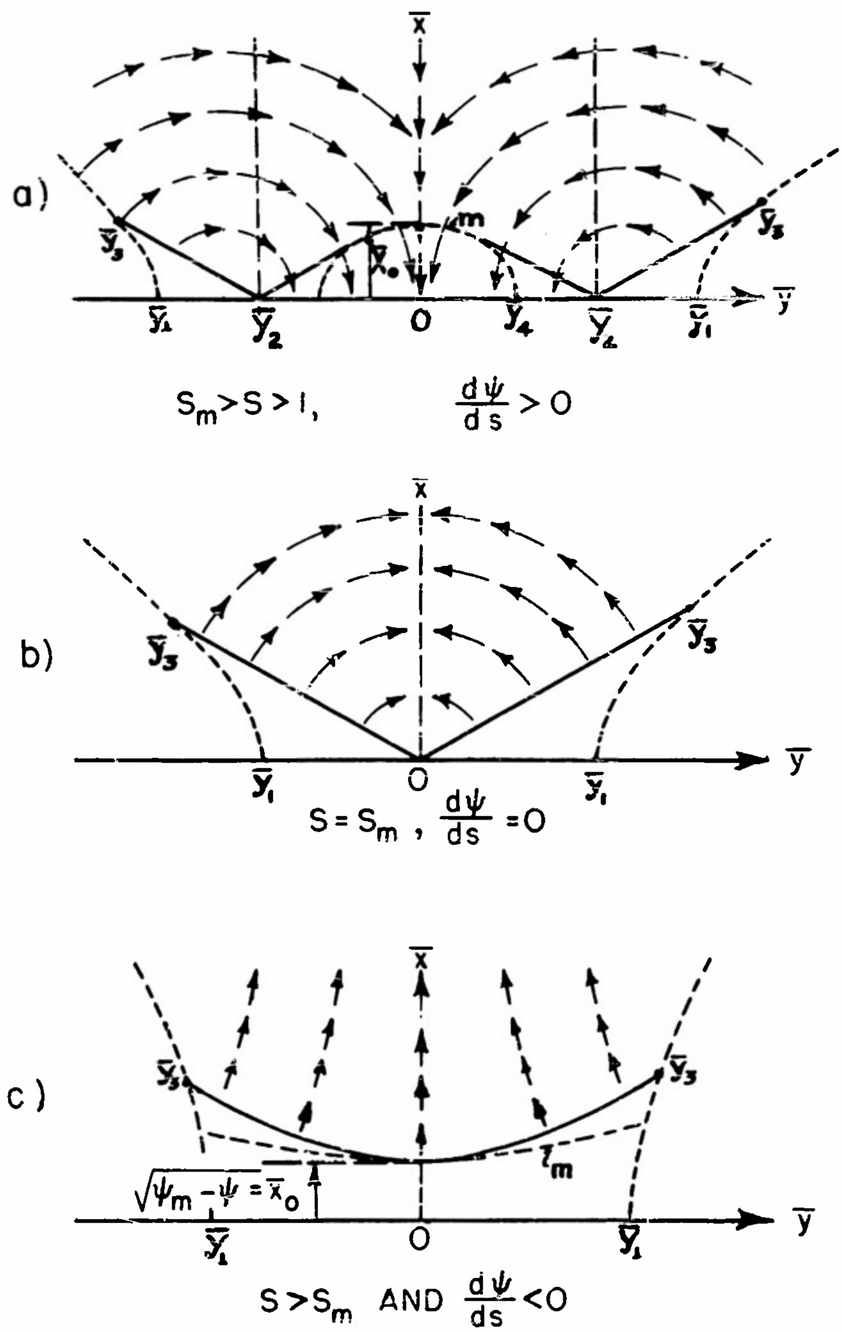

FIG.2-1 FLOW PATTERNS AND BOUNDARY OF W

$$\frac{\partial \bar{x}}{\partial s} = 0 , \quad \bar{y}_2 \equiv \pm \sqrt{\frac{s d\psi}{ds}} , \quad s < s_m . \tag{2.17}$$

We may now consider briefly the other sections of Fig. 2-1. In each one the vectors $\underline{t}$, indicated by the arrows in direction, but not in magnitude, give the pattern of flow for a particular radius s. The pattern is symmetric about the origin, but at $s = s_m$ all along the $\bar{x}$-axis there is a change from downward to upward flow. The points $\bar{y}_1$ and $\bar{y}_3$ have the same significance in all three sketches. In the second sketch the points $\bar{y}_2$ have closed together on the origin and the region of double cells under $\underline{m}$ has vanished. The points $\bar{y}_1$ also tend to close on the origin, and actually meet there when ψ is zero and $s \geq 2 s_m$. Hence the scale of the third sketch represents a considerable enlargement of the scale used in the first two. In this last sketch the region above the origin out to $\bar{x}_o$ is also excluded from W and lies in the shadow of the virtual cathode.

The points $\bar{y}_3$, it is clear from their definition, never close together. A rough approximation to W would then be a rectangle bounded by a horizontal line through $\bar{x}_o$ and vertical lines through $\bar{y}_3$. A still cruder approximation is the common one [2] which takes for W the entire half plane bounded below by $\bar{x} = \bar{x}_o$. This yields for S the following formula, in which the plus sign applies to the interval $r_c < r < r_m$:

$$S(r) = \frac{1}{2} \exp\left[-\psi(r)\right] \cdot \left[1 \pm \operatorname{erf} \left| \bar{x}_o \right|\right] , \quad \bar{x}_o \equiv \sqrt{\psi_m - \psi(r)} . \tag{2.18}$$

Here erf is the error function or probability integral, given, for instance, in Peirce's tables [4]. For a planar cathode W has no wings and $\underline{m}$ is indeed the line through $\bar{x}_o$ parallel to the $\bar{y}$-axis, so (2.18) is an exact relation, with ψ a function of the cartesian coordinate perpendicular to the cathode. To find S more precisely for a given cylindrical cathode, one may use numerical methods, or semi-analytic forms for an under- and an over-estimate of S, as Wheatcroft does.

The net outward current through a cylindrical surface, concentric with the cathode and of radius r, must be independent of r and will be given by an integral $I_a = \iint_{W_i} dI$. Here dI is defined in (2.9) and W_i is the region

W of the $(\bar{x},\bar{y})$-plane, minus the section, if any, which counts twice in S. W_i and di must change with radius so as to keep I_a constant. A rough approximation for I_a can be deduced from Fig. 2-1b:

$$I_a \doteq I_o \left\{ \sqrt{s}\ \mathrm{erf}\left|\bar{y}_1\right| \cdot \exp(-\psi) + 1 - \mathrm{erf}\left|\sqrt{s}\ \bar{y}_1\right| \right\} \Bigg|_{s=s_m} \tag{2.19}$$

This gives too large a value for I_a, because it includes in W_i the two triangular regions with corners at $\bar{y}_3$, $\bar{y}_1$, and $\bar{y}_2 = 0$.

If the anode voltage is made sufficiently negative, the barrier potential ψ_m moves radially out to the anode and disappears. Then if ψ_a and s_a are substituted in (2.14) for ψ_m and s_m, Fig. 2-1a will represent W for all values of r, $r_c < r < r_a$. Schottky studied thermionic currents flowing against such a retarding potential, and (2.19), evaluated for $s = s_a$, is his formula for I_a [1]. It still includes extra triangular regions $(\bar{y}_3, \bar{y}_1, \bar{y}_2)$, but in Fig. 2-1a these are far from the origin and introduce small error into I_a. Indeed, if $|y_1|$ is larger than 2, (2.19) reduces, with an error under 1 per cent, to:

$$I_a = I_o \sqrt{s} \exp(-\psi) \Bigg|_{s=s_a} . \tag{2.20}$$

Schottky's formula, we note parenthetically, is often quoted for very large s_a (or very small cathode radius) [5, page 80]. In this case, $\sqrt{s}\ \mathrm{erf}\left|\bar{y}_1\right|$ approaches $2\sqrt{\psi_a/\pi}$ and $\mathrm{erf}\left|\sqrt{s}\ \bar{y}_1\right|$ approaches $\mathrm{erf}\sqrt{\psi_a}$, but these forms do not apply in our diode.

In the next chapter we give results of a numerical calculation based on the true boundaries of W, the solid lines in Fig. 2-1. To complete here the formulation which will be used in this calculation, we require the potential ϕ to satisfy Poisson's equation (1.16). This we now write with one initial condition and normalizing definitions like (2.2) and (2.11):

$$\psi'' = -\frac{1}{2}[\exp(\alpha + 2\xi)] \cdot S(\xi) , \quad \psi' \equiv \frac{d\psi}{d\xi} , \quad \xi \equiv \frac{1}{2} \ln s ; \tag{2.21}$$

$$\psi_c \equiv \psi(\xi = 0) = 0 , \quad \exp(\alpha) \equiv \frac{2eI_o r_c}{\pi h \epsilon_o kT} \sqrt{\frac{\pi m}{2kT}} , \quad \psi \equiv \frac{e\phi}{kT} . \tag{2.22}$$

c. Integration Methods and I_o.

In this section we use the formulation developed above to interpret some data obtained from our diode. With Boltzmann's approximation, $S(\xi) = \exp[-\psi(\xi)]$, one can integrate (2.21) and obtain the results in Fig. 2.2. This approximation is a good one, as we noted following equation (2.14), in most of the interval $r_c < r < r_m$. Introducing it, we put (2.21) in the form:

$$\frac{d}{df}(f')^2 = \exp(f) \quad , \quad f \equiv \alpha + 2\xi - \psi \quad , \quad f' \equiv \frac{df}{d\xi} \tag{2.23}$$

One may show by substitution that a solution of (2.21) is:

$$\exp(f) = b^2 \cos^{-2}(a + \frac{b}{2}\xi) \quad , \text{ or}$$

$$\psi(\xi) = 2\xi + 2 \ln \cos(a + \frac{b}{2}\xi) - 2 \ln \cos a \tag{2.24}$$

The parameters $\underline{a}$ and $\underline{b}$ in (2.24) depend on $\exp(\alpha)$ and on f'_c, the subscript $\underline{c}$ referring to the cathode at $\xi = 0$:

$$b = \cos a \,[\exp(\alpha/2)] \quad , \quad f'_c = \sin a[\exp(\alpha/2)] \quad . \tag{2.25}$$

Here $\exp(\alpha)$ represents the parameter of emission current I_o (2.22), and f'_c represents the electric field at the cathode: $f'_c = 2 + (erE/kT)_c$. We note in (2.24) that $\psi(\xi)$ satisfies $\psi_c = 0$, as it should. The second condition on ψ is that it have a maximum at ξ_m, or that $f'_m = 2$. These two conditions permit one to determine $\underline{b}$ as an eigenvalue of (2.23), and by further algebra one obtains the results in Fig. 2-2.

The ordinate in Fig. 2-2 is the height of the potential barrier ψ_m, and the abscissa k_m describes its radial position r_m: $k_m = (s_m - 1)\cdot(s_m + 1)^{-1}$. The solid lines are contours of constant α. If they had been drawn in, contours of ψ'_c would be almost parallel to the contours of α; actually ψ'_c is represented by occasional underlined numbers on the α-contours. The light dashed contours I_a/I_o were calculated by (2.20), evaluated at s_m. Hence they have the triangular inaccuracy mentioned for (2.19). However, setting $\operatorname{erf}|\bar{y}_1| = 1$, as we did in (2.19) to obtain (2.20), introduces additional errors in I_a/I_o only in the region of heavy dashed contours $A = \operatorname{erf}|\bar{y}_1|$.

Since $S(\xi)$ must lie between $\exp(-\psi)$ and $\frac{1}{2}\exp(-\psi)$ in the interval $0 < \xi < \xi_m$, an upperbound in α to the error introduced by the Boltzmann approximation is $\ln 2 \doteq 0.7$. This is about half the α-interval used in Fig. 2-2. The position of each α-contour relative to its neighbors is much more accurate. The points numbered 1 through 5 near the origin, $k_m = \psi_m = 0$, represent a calculation for $\alpha = 10$ based on (2.18), and the position of the dashed line joining them, relative to the solid contour $\alpha = 10$, indicates the accuracy of this contour. Computations to improve Fig. 2-2, although it applies to any cylindrical diode and has some general interest, do not seem justified while a larger uncertainty remains in the experimental values of $\alpha(T)$.

Figure 2-3 presents, in the line through the points x, our data on the function $\alpha(T)$. The points are based on I_o extrapolated from curves of temperature limited current, and on T from curves of current in a retarding field, Figures 5-3 and 5-4 of T.R. 185. The parameter in Fig. 2-3 is V_f, the voltage applied to the cathode heater. The extrapolations to I_o above $940^\circ K (V_f = 12)$ are uncertain; and values of T below $820^\circ (V_f = 8.5)$ are merely estimates, so the points x become lines indicating a bracket on $\alpha(T)$. For instance, the point $V_f = 12$v, with $\alpha = 9.55$ and $T_c = 940^\circ K$ corresponds to 0.89 ma per cm^2, emission current density and 0.63 watts per cm^2, heater power. In terms of these quantities one can find the point on a conventional power-emission chart [6, Fig. 11, page 83]. The values appear reasonable.

Now I_o is measured with high anode voltages V_a, and T with increments ΔV_a, so the cathode and anode work functions, V_c and V_w, scarcely affect I_o, T or the points $\alpha(T)$. (One may perhaps question the combining of high and low voltage cathode characteristics in a single parameter.) The line Y in Fig. 2-3, on the other hand, and the curves in Fig. 2-4 use only data on the diode current in a retarding field and yield estimates of V_w and $V_c - V_w$. For Y, data from the linear portion of the curves in Fig. 5-4, T.R. 185, were used (chiefly the intersection $V_a(T)$ of each curve with the line $I_a = 1$ microampere). The formula for Y comes by eliminating I_o between Schottky's equation (2.20) and Richardson's equation [7, pages 25 to 47]:

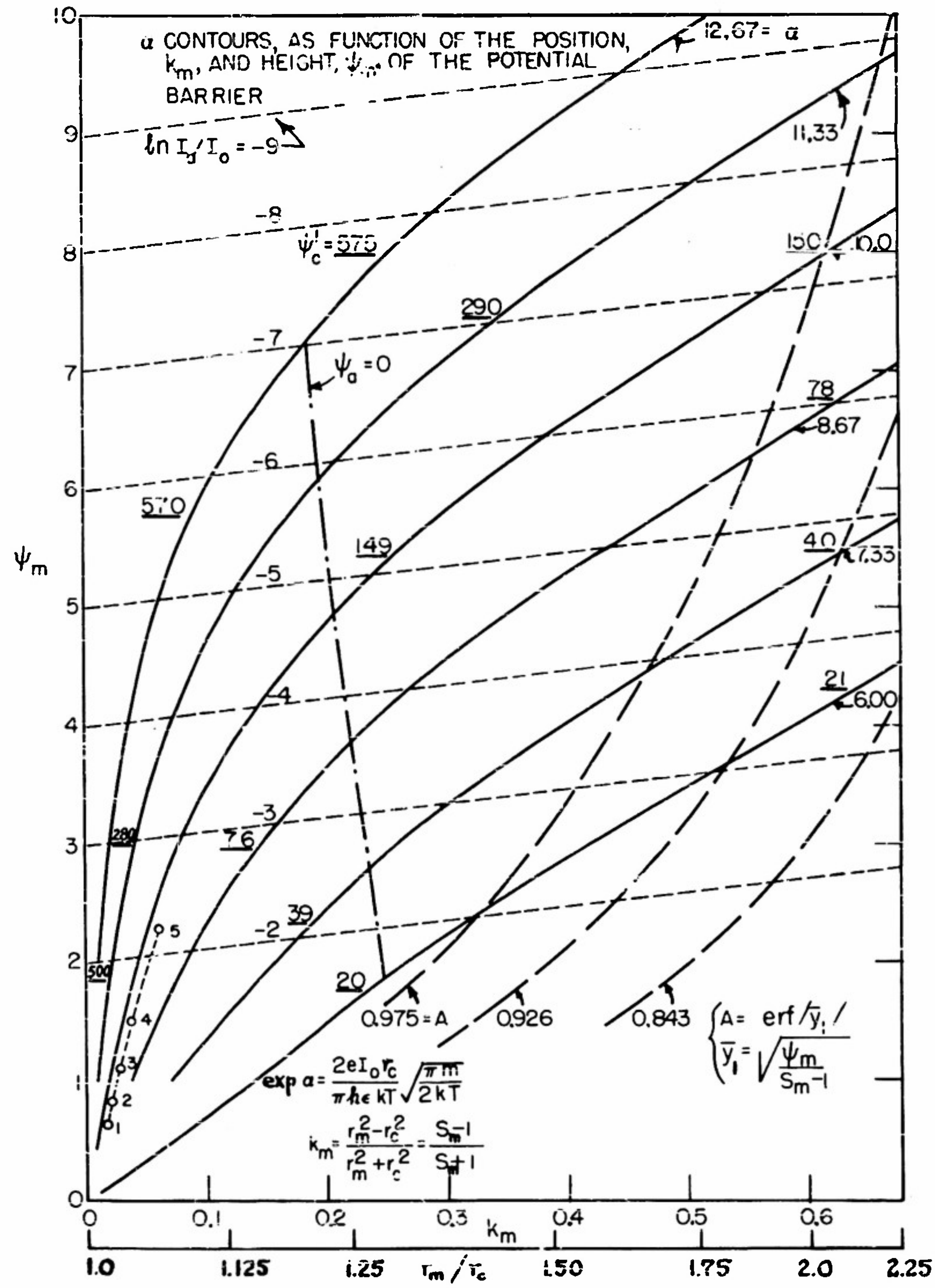

FIG. 2-2 INTEGRATION OF EQUATIONS FOR A THERMIONIC DIODE

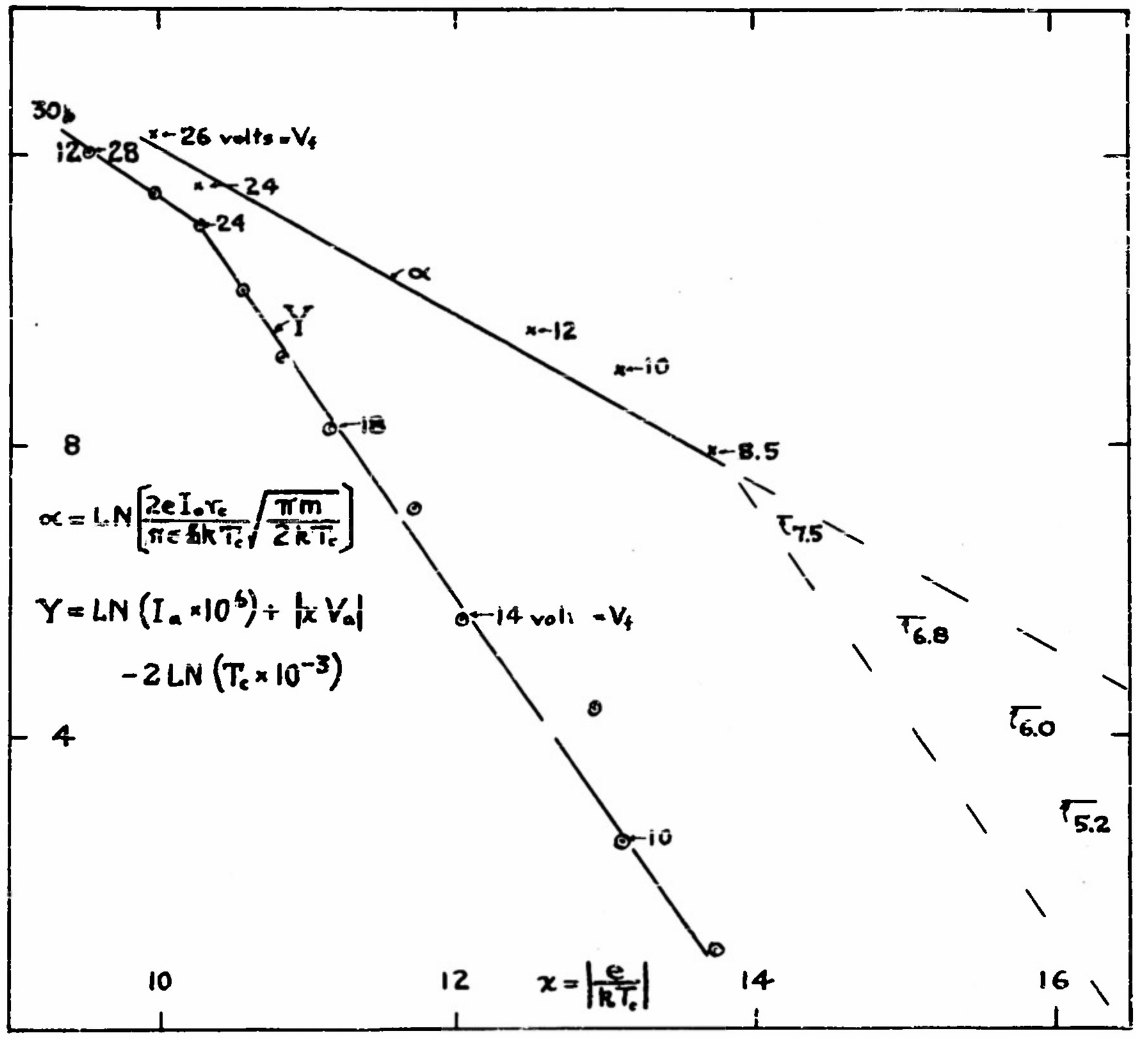

FIG 2-3 EMISSION PARAMETERS, α AND Y(x)

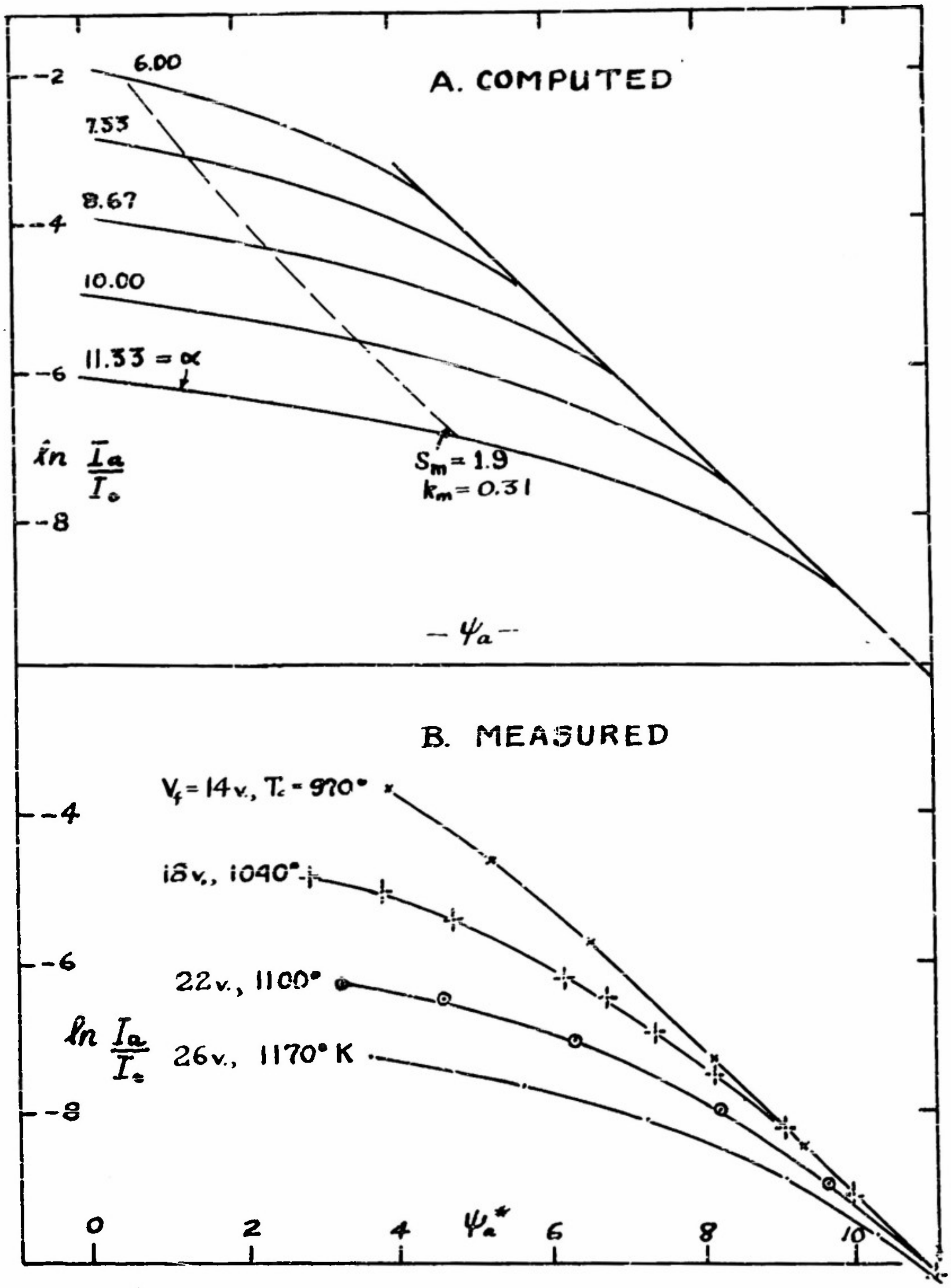

FIG 2-4 DIODE CURRENT FOR SMALL $\psi_a = eV_a/kT$.

$$I_c = A T^2 \exp\left\{-eV_c / kT\right\} \tag{2.26}$$

If the coefficient A here is independent of T, then Y is a linear function of T^{-1}:

$$\begin{aligned} Y &\equiv \ln I_a(x) + 2 \ln|x| + |x V_a| , \\ &= -x(V_c - V_w) + \ln[A\sqrt{s_a}\,(e/k)^2] , \\ &= a + |x V_w| + \tfrac{1}{2}\ln|x| - 10.96 \;;\; x \equiv (e/kT) \end{aligned} \tag{2.27}$$

Here the number 10.96 represents

$$\ln\left\{\frac{2r_c}{\pi h \epsilon}\sqrt{\frac{\pi m}{2e}}\right\} .$$

The points $Y(T, V_f)$ fall on portions of two lines which meet in V_f = 24 volts. One finds A in amps/cm$^2/^\circ$K from the intersection of Y(x) (extended) with x = 0, and $V_c - V_w$ in volts from the slope dY/dx. From the upper line, we find $10^{-2} > A > 10^{-3}$ and $1.5 > V_c - V_w > 1.3$, both reasonable values; but from the lower line (V_f = 24 to 10 volts) $A \doteq 27 \times 10^3$ and $V_c - V_w = 3.0$, quite impossible values [5, page 109]. The explanation may lie in heat losses through the ends of the cathode sleeve. These losses tend to overtake radiation losses at low values of T and may give the cathode a non-uniform temperature distribution. From comparing a and Y at V_f = 12, we find in (2.27), V_w = 0.26 volts.

Figure 2-4b reproduces portions of four curves of diode current against a retarding voltage (T.R. 185, Fig. 5-4). These curves have been tailored in two ways: The slope of each curve in its linear region was reduced to unity by choice of T in $\psi_a^* = e(V_a + V_w)/kT$, then each curve was made asymptotic to one line, the Schottky line (2.20), by choice of appropriate I_o. The I_o selected in this manner proves reasonably consistent with data on a in Fig. 2-3, but a correct selection depends critically on a correct value for V_w.

Normalization of V_a and I_a with respect to T_c and I_o has not changed the shape of the curves in Fig. 2-4b, however. Their topology resembles that of the curves in 2-4a, and these curves were computed from α-contours in Fig. 2-2. Each curve in Fig. 2-4a leaves the common asymptote, the Schottky line, when the virtual cathode lies just in front of the anode. As the retarding voltage ψ_a is reduced further, each curve in Fig. 2-4a may be considered the locus of a point $Q_\alpha(\psi_a)$, and a corresponding point $Q_\alpha^*(\psi_a)$ moves along a corresponding α-contour in Fig. 2-2 from $k_a = 0.675$ toward the cathode, $k = 0$. As $Q_\alpha^*(\psi_a)$ crosses contours of I_a/I_o in the direction of increasing I_a, so $Q_\alpha(\psi_a)$ moves up a curve in Fig. 2-4a toward higher values of $\ln(I_a/I_o)$, but $Q_\alpha(\psi_a)$ rises more slowly now than it did on the Schottky line. (This mental experiment with Q_α^* provides a key to the meaning of Fig. 2-2.) In Fig. 2-4a the curves end at $\psi_a = 0$ and the dot-dash line in Fig. 2-2 shows how far Q_α^* has come down the α-contour. Thus the line $\psi_a = 0$ in Fig. 2-2 represents the position of the virtual cathode, when anode and cathode are at the same potential.

The computations for Fig. 2-4a involved matching the solution of Poisson's equation (2.24) for $r_c \leq r < r_m$ to the Langmuir solution (1.23) for the interval $r_m < r \leq r_a$. We conclude this section with a brief examination of Langmuir's series as a solution of (2.21) for $r > r_m$. Beyond the virtual cathode, W takes the shape shown in Fig. 2-1c, and S takes the form

$$S(s) = \frac{1}{2\sqrt{\pi}} \int_{-\infty}^{\infty} d\bar{y}\,[1 - \operatorname{erf} \bar{x}(\bar{y})]\, \exp\left\{-(\bar{y}^2 + \psi)\right\} . \tag{2.28}$$

Here $\bar{x}(\bar{y})$ represents the solid curve between points $\bar{y}_3$ and $\bar{x}_o$ in Fig. 2-1c, plus dashed hyperbolic segments out toward large $\bar{x}_o$, so clearly $\bar{x}(\bar{y}) \geq \bar{x}_o$. If $\bar{x}_o$ is larger than 2, we may replace the error function in (2.28) by its asymptotic form:

$$S(s) = \frac{1}{2\pi} \int_{-\infty}^{\infty} d\bar{y}\, \frac{\exp\left\{-[\bar{y}^2 + \psi + \bar{x}^2(\bar{y})]\right\}}{\bar{x}(\bar{y})} \tag{2.29}$$

If we replace the solid curve bordering W by the dashed hyperbolic segment $\overline{m}$, $\bar{x}(\bar{y})$ along it is given by (2.14) and:

$$S(s) \leq \frac{\exp(-\psi_m)}{2\pi} \int_{-\infty}^{\infty} \frac{\exp\left\{-\bar{s y}^2 / s_m\right\} d\bar{y}}{\sqrt{\psi_m - \psi + \bar{y}^2 (\frac{s}{s_m} - 1)}} \quad . \tag{2.30}$$

Because $\left\{-\bar{y}^2\right\}$ appears in an exponent in (2.30), only small values of $|\bar{y}|$ count and we may neglect $\bar{y}^2(\frac{s}{s_m} - 1)$ in the denominator. Performing the integration we find:

$$S(s) \leq \frac{1}{2} \exp(-\psi_m) \cdot \left\{\frac{s_m}{s\pi(\psi_m - \psi)}\right\}^{1/2} \tag{2.31}$$

Substituting (2.31) in (2.21) with redefinitions we obtain:

$$\bar{\psi}' \doteq \exp(\bar{a} + \bar{\xi})(4\sqrt{\pi \bar{\psi}})^{-1} \quad , \quad \bar{\psi}' = d\bar{\psi}/d\bar{\xi} \quad ; \tag{2.32}$$

$$\bar{\psi} \equiv \psi_m - \psi, \quad \bar{\xi} \equiv \xi - \xi_m, \quad \bar{a} \equiv a + 2\xi_m - \psi_m \quad . \tag{2.33}$$

The series $f_L(\xi)$ in (1.23) is Langmuir's solution of (2.32), with initial conditions at r_m: $\bar{\psi} = 0$, $\bar{\psi}' = 0$, and $\psi \doteq d f_L^{4/3}$:

$$d^{3/2} \equiv 9 \exp \bar{a} / 16\sqrt{\pi} \text{ , or } d = 0.465 \exp(2\bar{a}/3) \quad . \tag{2.34}$$

The equation which Langmuir solved was originally derived for a space charge limited cylindrical diode in which the velocity distribution among electrons was ignored. It is, we find, the asymptotic form of Poisson's equation, including a Maxwellian distribution of emission velocities, when $\bar{\psi}$ is larger than four. Langmuir's solution is not necessarily asymptotic, for given ψ_m, to solutions arising from a more careful consideration of S(r) near r_m. It was used to represent $\psi(\xi)$ in the interval $\xi_m < \xi < \xi_a$, with the condition $\bar{a} = \alpha + \xi_m + \ln(I_a/I_o)$ to match it to the Boltzmann solution in the interval $0 < \xi < \xi_m$, and it yielded ψ_a for Fig. 2-4a. Its use is partially justified by the resemblances between the curves in Figs. 2-4a and 2-4b.

d. Summary

The space charge inside the virtual cathode in a thermionic diode depends on the emission current and temperature, I_o and T, and on one other parameter, such as ψ_c', ψ_m or r_m. The dependence of this third parameter on the anode voltage ψ_a can be found if the whole charge distribution even to the anode is known. I_o depends on the cathode material, surface area and temperature. The use of T as a parameter represents the well-founded assumption that the emission velocities have a Maxwellian distribution.

If the particles in the space charge do not interact individually, their entire orbits obey equations (2.3). These equations cut away the edges of the velocity distribution as the particles move out from the cathode. The shape of the edges determines the values of the integrals I(r) and S(r), the radial current and the charge density. S(r) determines the potential function $\psi(r)$ through Poisson's equation, and $\psi(r)$ through (2.3) in turn helps determine S(r). Space-charge problems usually include this circle of self-consistency.

Low anode voltages or negative ones which cause the virtual cathode to move out toward the anode, bring the whole tube in a sense within the cathode region. Hence they are used to examine the effects of cathode parameters, although I_o may also be found with high anode voltages, $\overline{\psi_a} \equiv \psi_m - \psi_a$. If $\overline{\psi_a}$ is high, the velocity the electrons pick up in the radial field far exceeds the distribution of thermal velocities. Then Langmuir's series solution, in which T and I_o are no longer important parameters, describes $\psi(r)$.

References in Chapter II

1. W. Schottky, "On the Emission of Electrons from Hot Wires in Retarding Potentials," Ann. Phys. Lpg. 44, 1011-1032 (1914).
2. I. Langmuir, "The Effect of Space Charge and Initial Velocities on the Potential Distribution and Thermionic Current between Parallel Plane Electrodes," Phys. Rev. 21, 419-435 (1923).
3. E.L.E. Wheatcroft, "The Theory of the Thermionic Diode," Proc. Inst. Elect. Engrs., Wireless Section, 15, 94-105 (1940).
4. B.O. Peirce, A Short Table of Integrals, Ginn and Co., Boston, 1929.
5. E.L. Chaffee, Theory of Thermionic Vacuum Tubes, McGraw-Hill, New York, 1933.
6. Members of the E.E. Staff, M.I.T., Applied Electronics, Wiley, New York, 1943.
7. Herrmann and Wagener, The Oxide-Coated Cathode, Vol. II, Chapman-Hall, London, 1951.

III

Effects of Emission Temperature in a Magnetic Field

a. Introduction

The problem of describing space charge in front of an emitting surface parallel to a steady magnetic field has apparently received little attention [1, page 211]. It is common to assume, in discussing magnetron performance, that the magnetic field has little or no effect on the virtual cathode. After considering the effects of the tangential component of electronic emission velocities, Twiss in 1953, it is true, proposed a drastic revision of conventional magnetron models, the so-called single and double stream models for the whole charge distribution from cathode to anode [2, pages 247 to 289]. But Twiss too failed to examine details of the charge distribution close to the cathode, and we shall not review his results here.

The magnetic field does in fact modify many features of the cathode region, as we shall find on extending the analysis of Chapter II. But the largest effects of the magnetic field occur in the Hull cutoff transition. We present a rough calculation of the thermal effects to be expected in this transition, and conclude this chapter with results of a numerical calculation. The results allow us to contrast some features of the cathode region before and after imposing a steady magnetic field.

b. The Virtual Cathode in a Magnetic Field.

To extend our previous analysis we adopt the same definitions s, ψ, $\overline{x}$ and $\overline{y}$ (2.2), representing the radial coordinate, the potential and the normalized electronic velocities in a cylindrical diode. We continue to ignore the effects of collisions and to suppress the z-coordinate. Moreover, we neglect possible effects of a magnetic field on the mechanism of emission and on properties of the cathode materials.

The steady magnetic field B, uniform and parallel to the system axis, z, we normalize with respect to kT:

$$\omega \equiv \frac{eB}{m} \; , \; h \equiv \frac{\omega}{2}\sqrt{\frac{mr_c^2}{2kT}} \; . \tag{3.1}$$

(We will avoid using in this chapter the symbol h as the axial length of the cathode.) This magnetic field does not enter the energy equation (2. 1), but the new momentum relation is (1. 15), $r^2(\dot{\theta} + \omega/2)$ = constant. Instead of (2. 3) we have:

$$\bar{x}^2 + \bar{y}^2 + \psi = x^2 + y^2 \quad , \quad \sqrt{s}\,\bar{y} + s\,h = y + h \qquad (3.2)$$

On eliminating y between these relations, we find:

$$\bar{x}^2 - x^2 + \chi(s) = (s-1)(\bar{y} + \sqrt{s}\,h)^2 \qquad (3.3)$$

Here $\chi(s)$ might be called an effective potential, $\chi(s) \equiv \psi + h^2(s-1)$, but convenience rather than any physical concept justifies its use.

The definitions of incremental charge density dS and current dI (2.4, 2.5), involving the energy relation, remain unchanged. The Jacobian of a transformation from emission velocity variables (x,y) to other velocity variables $(\bar{x},\bar{y})$ remains $\sqrt{s}$ (2.7). Hence dS and dI transform as before (2.9, 2.12). For the integral S(r), the region of integration W on the $(\bar{x},\bar{y})$-plane depends chiefly on one observation: for any electron in radial outward motion that contributes to S(r), its velocity $\bar{x}(r)$ must have been greater than zero from the cathode continuously to the radius in question. In other words, except perhaps for singular cases, the orbit equations allow each electron only one outer turning point. This observation leads us to define wings of the $(\bar{x}\bar{y})$-plane, excluded from W as before. We complete later the integration over electrons falling back to the cathode.

The features of W sketched in Fig. 3-1 should be compared with those sketched in Fig. 2-1. The hyperbolic segments $(\bar{y}_1, \bar{y}_3, \ldots)$ and the solid lines $(\bar{y}_3, \bar{y}_2)$ on the boundary of W have the same significance. The points themselves are given by formulae like (2.13, 2.17):

$$Y_1^2 = \chi/\overline{s-1} \;\; ; \;\; Y_2^2 = s\,(d\chi/ds) \;\; ; \;\; sY_3^2 = (d\chi/ds)_{1=s}$$

$$x = 0 = \bar{x} \qquad (\partial\bar{x}/\partial s) = 0 \qquad \text{(end of envelope)} \qquad (3.4)$$

These points $Y \equiv \bar{y} + \sqrt{s}\,h$ lie symmetrically about $\bar{y} = -\sqrt{s}\,h$ rather than about the origin $\bar{y} = 0$, and χ has replaced ψ. These differences, due to h, are clear already in (3.3). Reversing the direction of B merely changes

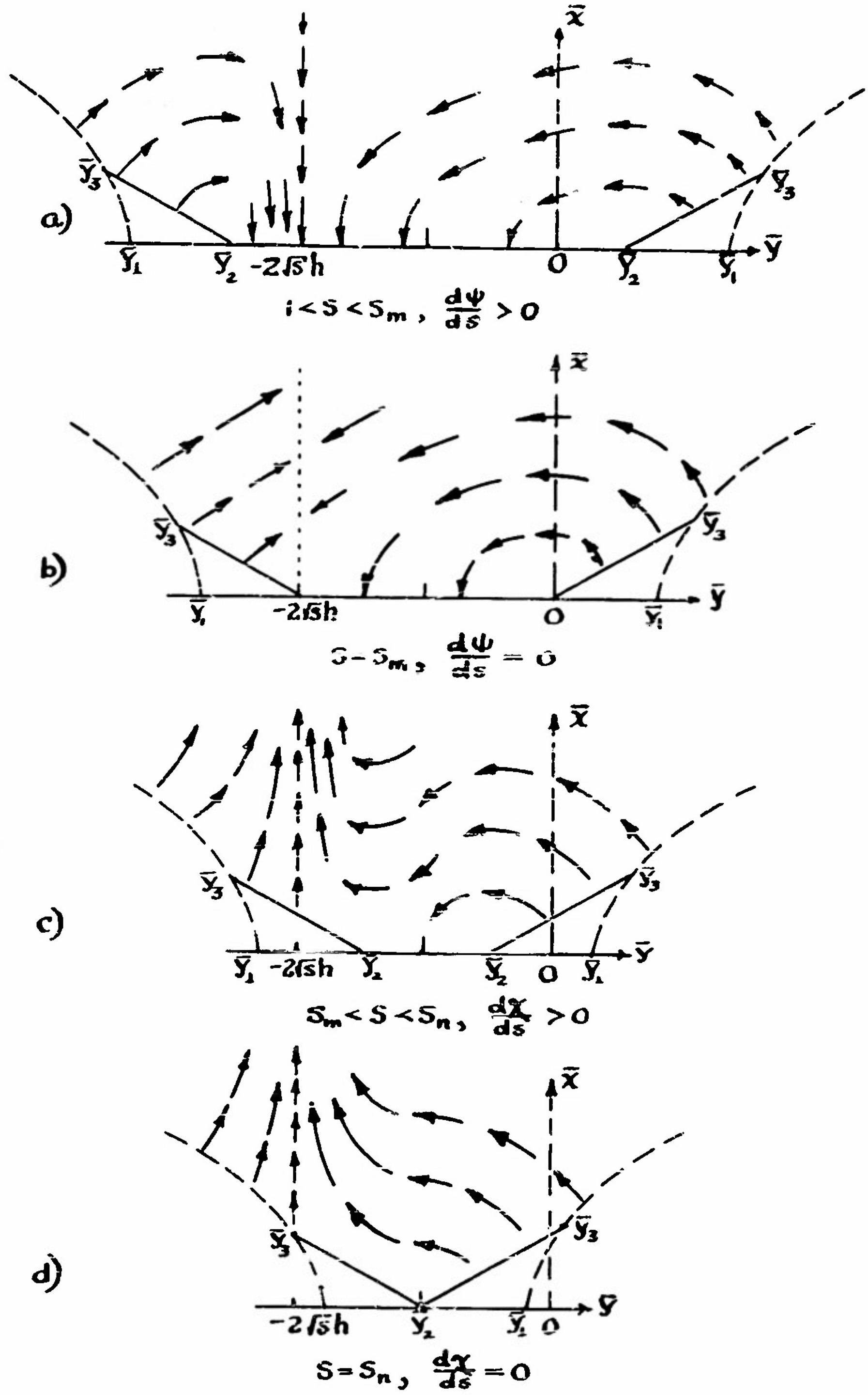

FIG. 3-1 FLOW PATTERN IN W, $h>0$

the sign of h, and causes the sketches in Fig. 3-1 to be reflected about the line $y = -\sqrt{s}\,h$. The flow vector $\underline{t}$, moreover, is now vertical above $y = -2\sqrt{s}\,h$ rather than above the origin (2.16).

$$\underline{t} = \frac{\hat{x}}{2\overline{x}}\left\{\frac{Y^2}{s} - \frac{d\chi}{ds}\right\} - \hat{y}\left(\frac{\overline{y}}{2s} + \frac{h}{\sqrt{s}}\right) \quad . \tag{3.5}$$

The contour bounding W near the origin of the $(\overline{x},\overline{y})$-plane is the most important one, since the integrand in S has the bell shape mentioned before, centered above the origin. At the virtual cathode where $d\psi/ds$ vanishes and s equals s_m, the boundary touches the origin from one side only (Fig. 3-1b). It cuts from W more of the $(\overline{x},\overline{y})$-plane at the origin as s increases beyond s_m. However, in part of W the downward flow continues out beyond s_m to a second radius s_n where the points $\overline{y}_2$ meet and $d\chi/ds$ vanishes (Fig. 3-1d). Beyond s_n all downward flow ceases, but between s_m and s_n some electrons which have passed the virtual cathode are reflected by the magnetic field and fall back to the cathode surface. Hence in the presence of a magnetic field s_n replaces s_m as the top of the cathode barrier. This is in spite of the fact that s_n lies in a region of accelerating electric field, given by $E(r_n) = m\omega^2 r_n/4e$.

The solid curve $(\overline{y}_2,\overline{y}_3)$ near the origin is the only boundary of W we shall have to find in calculating S(r). The equations for this line were based on mapping a series of lines $\overline{x}(s*) = 0$ on to the (x,y)-plane with $P^{-1}(s*)$ and remapping the envelope of the family of elliptic segments thus obtained back on to a particular $(\overline{x},\overline{y})$-plane with P(s) (Chapter II). In these equations then s is fixed and s* variable, but s* lies inside of s:

$$sY_e(s*)^2 = (s^2\, d\chi/ds)_{s*} \quad , \quad \overline{x}_e^{\,2}(s*) = \chi(s*) - \chi(s) + \frac{s-s*}{s}(s\,d\chi/ds)_{s*} \tag{3.6}$$

The tangent to the solid curve at $\overline{y}_2$, $d\overline{x}_e/d\overline{y}_e$, is real as long as $d^2\chi/ds^2$ is negative and $d\chi/ds$ positive:

$$(d\overline{x}_e/d\overline{y}_e)^2 = -\left\{1 + \frac{s}{2}\frac{d^2\chi}{ds^2}\bigg/\frac{d\chi}{ds}\right\}^{-1}_{s*=s} \tag{3.7}$$

Clearly, to find the boundary of W at s, we must know the function $\chi(s*)$ and its derivatives in the whole interval $1 \leq s* \leq s$.

The corresponding formulae for a planar magnetron are rather less simple and symmetric. We record them as the basis for one further comment on s_n: Placing the planar cathode (the reference for potential, $\phi_c=0$) at a height x_c above the (y,z)-plane in order to normalize with reference to x_c, rather than to the anode height d, we introduce planar definitions like (2.2):

$$s = (x/x_c) \quad , \quad \psi = \frac{e\phi}{kT} \quad , \quad \bar{u} = \dot{x}\sqrt{\frac{m}{2kT}} \quad , \quad \bar{v} = \dot{y}\sqrt{\frac{m}{2kT}} \tag{3.8}$$

The uniform magnetic field B, parallel to the z-axis, appears in:

$$\omega \equiv eB/m \quad , \quad h = \frac{\omega}{2}\sqrt{\frac{mx_c^2}{2kT}} \tag{3.9}$$

The orbit equations for an electron after emission are:

$$\bar{u}^2 + \bar{v}^2 + \psi(s) = u^2 + v^2 \, , \quad \bar{v} + hs = v + h \quad . \tag{3.10}$$

After eliminating v, we obtain a relation like (3.3), especially if y in (3.3) is much less than $\sqrt{s}\,h$:

$$\bar{u}^2 - u^2 + \chi = (s-1)\,h\,[2\bar{v} + sh] \quad , \quad \chi \equiv \psi + h^2(s-1) \quad . \tag{3.11}$$

From the resemblance of (3.11) to (3.3), $|\bar{y}| \ll \sqrt{s}\,h$, it follows that in the important region near the origin on the $\bar{x}\bar{y}$- and the $(\bar{u},\bar{v})$-planes, the curves bounding W are almost identical. The planar formulae for $\bar{v}_1$, $\bar{v}_2$, $\bar{v}_e$, $\bar{u}_e^2$ and t, moreover, resemble the cylindrical ones if one assumes $\psi \ll h^2(s-1)$ and expands χ in (3.4, 3.5, and 3.6).

Away from the origin, however, (3.11) leads to a parabola, and the envelope of mappings $P^{-1}(s*)(\bar{u}=0)$ is an unbounded curve tangent to a family of parabolae on the (u,v)-plane. Hence the vanishing of $(d\chi/ds)$ does not define a release height in a planar magnetron. We conclude that one can overemphasize the importance of s_n in a cylindrical diode. The eclipse of the origin by the curve $(\bar{y}_2\bar{y}_3)$, as we saw, begins at s_m and relatively few electrons fall back to the cathode from radii between s_m and s_n.

As one increases the magnetic field in a cylindrical diode, the release radius moves out and the Hull radius contracts, so eventually these radii may merge. Before this happens, however, our present analysis fails because it ignores the effects of collisions and the stable orbits within the cathode region into which electrons may be pushed and trapped. To integrate $S(r)$ over the electrons falling back to the cathode as well, we must distinguish two cases. For a diode in the regime before cutoff the release radius helps fix the boundary around cells $d(x)\,dy$ in W which count twice. After cutoff, the anode radius determines this boundary, and virtually all cells lying within W count twice.

c. The Cutoff Transition.

Before cutoff, in other words before θ_a reaches 2π (Fig. 1-1), some electrons which were released from r_n with unfavorable tangential velocities fail to reach the anode. They are then lost to the anode current I_a and in completing their paths back to the cathode they contribute a double shielding effect. For both reasons they cause I_a to decrease, yet the analysis in Chapter I took no account of such electrons. As the magnetic field increases through its critical value, an ever-increasing proportion of the radial current I_n through r_n misses the anode. This transition is, of course, the Hull cutoff. We now wish to extend the W integration clear to the anode and find the ratio I_a/I_n as a function of p. We consider that cutoff begins where this ratio starts to fall below one, at $p = p_i$.

Figure 3-2 may clarify the argument. The first sketch represents the plane of emission velocities (x,y): the solid curve is the envelope of the family of elliptic segments $\overline{x}(\overline{s}) = 0$, and the ellipse $\overline{x}(s_n) = 0$ touches it at $y = h$. The second sketch represents the velocity distribution at the release radius s_n: the solid curve inside $\overline{y}_3$ represents the envelope, and the $\overline{y}$-axis is the dashed ellipse in the previous sketch. The third sketch is an enlargement of the area near the origin in the second one. The fourth sketch is of this same area, referred to axes (u,v) which are aligned with the boundary of W near the origin, and hence lie at some angle γ to the $(\overline{x},\overline{y})$-axes.

In each sketch the dot-dash curves represent the condition $\overline{x}(s_a) = 0$. In the first and second ones a single such curve appears, an elliptic segment, with the equations:

$$x^2 + (1 - \frac{1}{s_a})(y + h) = \chi(s_a) = h^2(s_a - 1 - 8p) \text{ in 3-2a }, \qquad (3.12)$$

$$\overline{x}^2 + (1 - s_n/s_a)(\overline{y} + \sqrt{s_n}\,h)^2 = \chi(s_a) - \chi(s_n) \text{ in 3-2b }. \qquad (3.13)$$

This curve passes through W only if $\chi(s_a)$ is larger than $\chi(s_n)$; hence the definition of p_i is:

$$p_i \equiv \frac{1}{8}(s_a - s_n), \text{ if } |\Phi(s_n)| << p_i \quad , \quad \chi(s_a) = \chi(s_n) \quad . \qquad (3.14)$$

(Apparently, in a planar magnetron p_i like s_n moves to infinity, and the smallest magnetic field reflects some electrons from all heights x back to the cathode.) When p equals p_i, we assume that s_n still lies fairly close to the cathode. The second derivatives of ψ and χ must vanish between s_n and s_a, and both curves must have inflection points. In fact, while $|\psi|$ beyond s_m is a monotomic increasing function of s, $\chi(s)$ behaves more like a polynomial cubic in s.

In the third and the fourth sketches three dot-dash curves represent a corner of the elliptic segment (3.13) for three successive values of p. Now in fact changing p will change the whole function $\chi(s)$ and with it the solid line bounding W, but we have to assume these changes are small compared to the movement of the curve $\overline{x}(s_a) = 0$. This means we regard I_n as fixed during the cutoff transition and ignore the extra shielding of the virtual cathode by electrons whose velocities at s_n place them inside the dot-dash curve $\overline{x}(s_a) = 0$.

From Fig. 3-2c the current increment dI(u,v) and from Fig. 3-2d the integral I_n over the half plane can be written by inspection:

$$dI = I_o \sqrt{\frac{s_n}{\pi}} \exp\left\{-(\psi_n + u^2 + v^2)\right\} [\cos\gamma \, d(u^2) dv + \sin\gamma \, du \, d(v^2)] \quad ; \quad (3.15)$$

$$I_n = I_o \sqrt{s_n} \exp\left\{-(\psi_n + u_o^2)\right\} \cos\gamma \quad .$$

Here u_o is the distance along the u-axis from the origin to the edge of W_n.

The current I_a has the same increments as I_n, but the area of integration W_a is reduced from W_n by removing the cells under the dot-dash curve. This curve cuts the v-axis at v_n. We take v_n as the v-coordinate also of the intersection of the dot-dash curve with the solid edge of W_n. As p decreases, the ellipse $\overline{x}(s_a) = 0$ grows and v_n sweeps across the origin. Our problem is to make explicit the dependence of I_a on p from the formula:

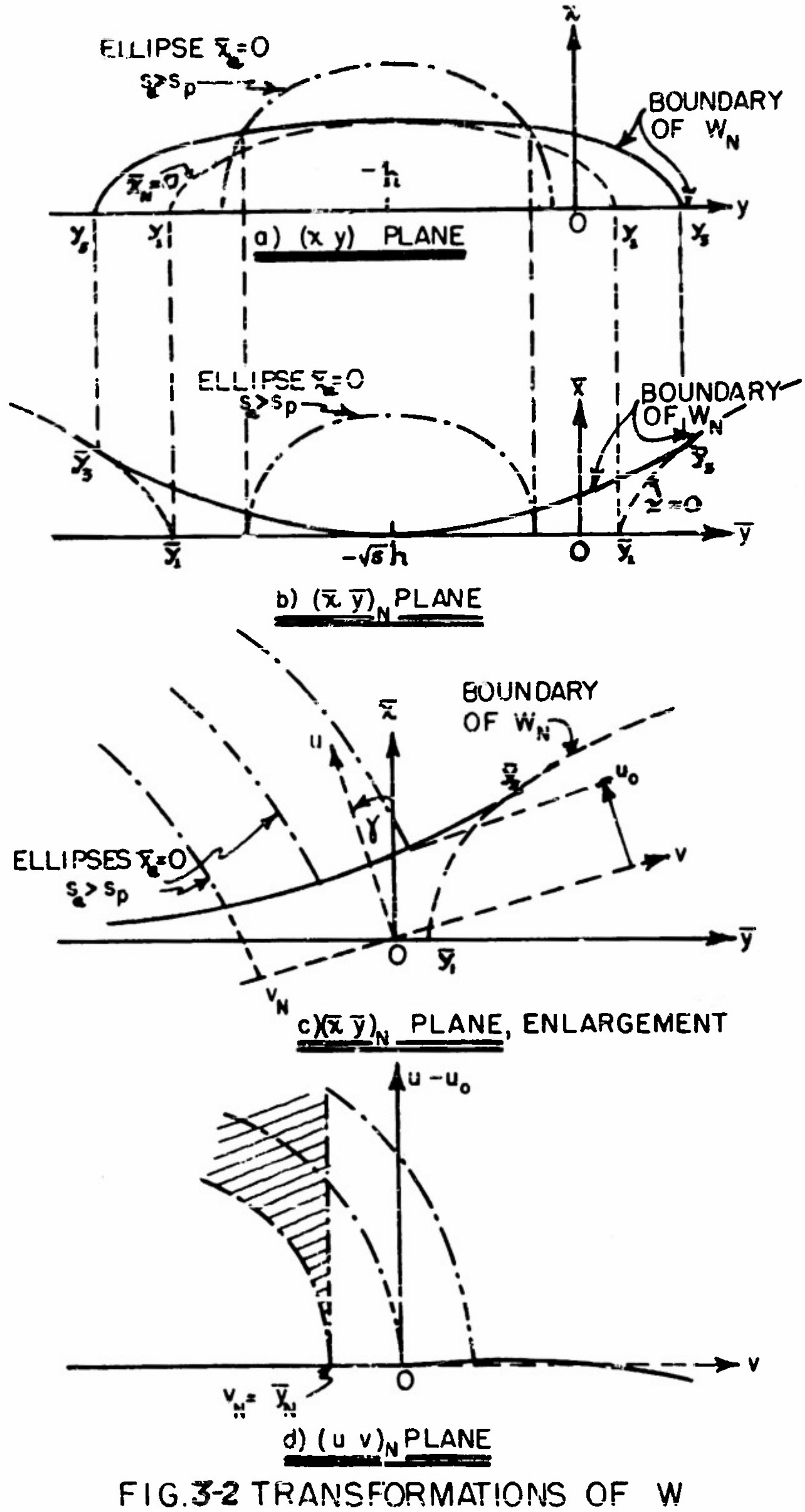

FIG. 3-2 TRANSFORMATIONS OF W

$$I_a = \frac{I_o}{2}\Big[\sqrt{s_n}\exp(-\psi_n)\Big\{\exp(-u_o^2)\cos\gamma\,(1 \pm \mathrm{erf}\,|v_n|) +$$

$$\exp(-v_n^2)\sin\gamma\,(1 - \mathrm{erf}\,u_o)\Big\} + \sqrt{s_a}\exp(-\psi_a)(1 - \mathrm{erf}\,|\bar{y}_a|)\Big] \qquad (3.16)$$

(If v_n is less than zero, we choose the plus sign before erf $|v_n|$, etc.) The last term in (3.16) represents the shaded area in Fig. 3-2d. The change, $P(s_a)(\bar{x},\bar{y})(s_n) = (\bar{x},\bar{y})(s_a)$, to velocity variables at the anode, maps the dot-dash curve into the $\bar{y}(s_a)$-axis and yields this term.

The formula used to compute the two curves in Fig. 3-3 contains only the expressions K and $\bar{y}_n$; it is:

$$\frac{I_a}{I_n} = \frac{1}{2}\left\{(1 \pm \mathrm{erf}\,|\bar{y}_n|) + \frac{\exp(-\bar{y}_n^2)}{h\sqrt{\pi}(1-K)}\right\} \qquad (3.17)$$

To derive it from (3.15) and (3.16) we first assume, in view of our ignorance of the exact shape of W_n, that γ and u_o are zero and v_n equals $\bar{y}_n$. Then we have:

$$\frac{I_a}{I_n} = \frac{1}{2}\left\{(1 \pm \mathrm{erf}\,|\bar{y}_n|) + \exp(\psi_n - \psi_a)\sqrt{\frac{s_a}{s_n}}(1 - \mathrm{erf}\,|\bar{y}_a|)\right\} \qquad (3.18)$$

We define $\bar{y}_n$ by setting $\bar{x}^2 = 0$ in (3.13) and dropping $\Phi(s_n)$ as in (3.14):

$$\bar{y}_n \equiv \sqrt{s_n}\,h\left\{-1 + \sqrt{\frac{s_a}{s_n}}\sqrt{1 - \frac{8p}{s_a - s_n}}\right\}. \qquad (3.19)$$

The point representing $\bar{y}_n$ on the $(\bar{x},\bar{y})(s_a)$-plane is $\bar{y}_a$:

$$\bar{y}_a \equiv \sqrt{s_a}\,h\left\{-1 + \sqrt{\frac{s_n}{s_a}}\sqrt{1 - \frac{8p}{s_a - s_n}}\right\} \equiv \sqrt{s_a}\,h\left\{-1 + K\right\} \qquad (3.20)$$

Whenever $\bar{y}_n$ is near zero, $\bar{y}_a$ is less than zero and $|\bar{y}_a|$ is larger than one ($K \doteq s_n/s_a < 0.2$), so we can write:

$$1 - \mathrm{erf}\,|\bar{y}_a| \doteq \left\{\exp(-\bar{y}_a^2)\right\}(\pi\bar{y}_a^2)^{-1/2} \qquad (3.21)$$

Finally, from the energy relation (3.2) with $\bar{x}(s_a) = 0 = \bar{x}(s_n)$, we have:

$$\psi(s_a) + \bar{y}_a^2 = \psi(s_n) + \bar{y}_n^2 \tag{3.22}$$

Thus we arrive at (3.17), giving I_a/I_n as a function of p and h. The center of the cutoff transition occurs when $\bar{y}_n$ is zero, and this defines $p_c < p_i$:

$$p_c = \frac{(s_a - s_n)^2}{8 s_a} \doteq \frac{(s_a - 1)^2}{8 s_a} \quad \text{since } s_a \gg s_n \doteq 1 \ . \tag{3.23}$$

In general, the two curves in Fig. 3-3 show how much a distribution in emission velocities would tend to round off a transition through cutoff, if the current I_n through the cathode barrier could be fixed while the magnetic field increased or p decreased. Actually I_n is not fixed. One might expect I_n to fall by half in the transition, since electrons which double back from anode to cathode roughly double their contribution to shielding the virtual cathode.

The curves in Fig. 3-3 should be multiplied by I_n/I_L before standing comparison with the data in Fig. 3-4. If I_n/I_L also decreased in the cutoff transition, the calculated curves would be sharper than 3-3, but we find the data in Fig. 3-4 shows rather a less abrupt cutoff. This suggests that another transport mechanism, associated perhaps with collisions between charges moving radially in and out, affects the shape of the transition.

The data in Fig. 3-4 for the regime before cutoff, from p = 10 to $p_i \doteq 0.55$ is in qualitative agreement with the transit time effects calculated for Fig. 1-1. On the other side of p_i, the curve $V_a = 100$ in Fig. 3-4 is more abrupt than the curves $V_a = 2.5$; indeed, the angle between them is larger than between the calculated curves in Fig. 3-3. Of the two curves $V_a = 2.5$, the one taken with the hotter cathode ($T_c = 1230^\circ$K, $V_f = 30$) as we would expect is slightly more rounded near $p = p_i$ than the other ($T_c = 1130^\circ$, $V_f = 24$ volts). To make the curves $V_a = 100$ and $V_a = 2.5$ cross near p_c, 0.75 volts was added to the potential applied to the tube in calculating p. We saw in Chapter II that $V_c - V_w$ had this sign and perhaps twice this magnitude.

d. A Numerical Example

In this section we show by numerical work the dependence of the cathode

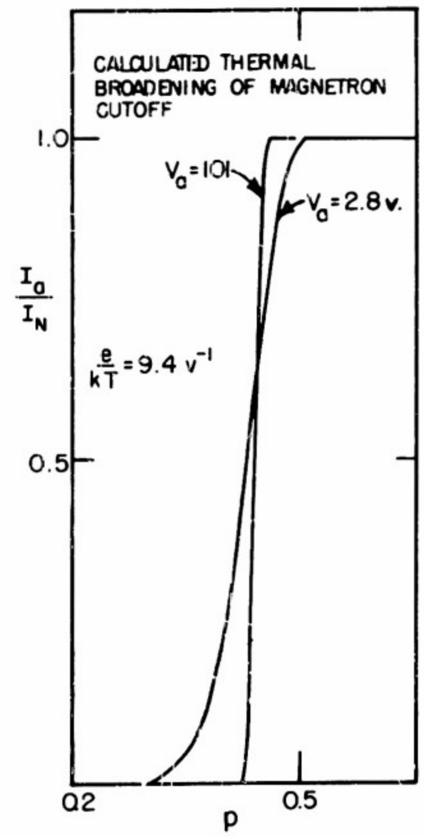

FIGURE 3-3

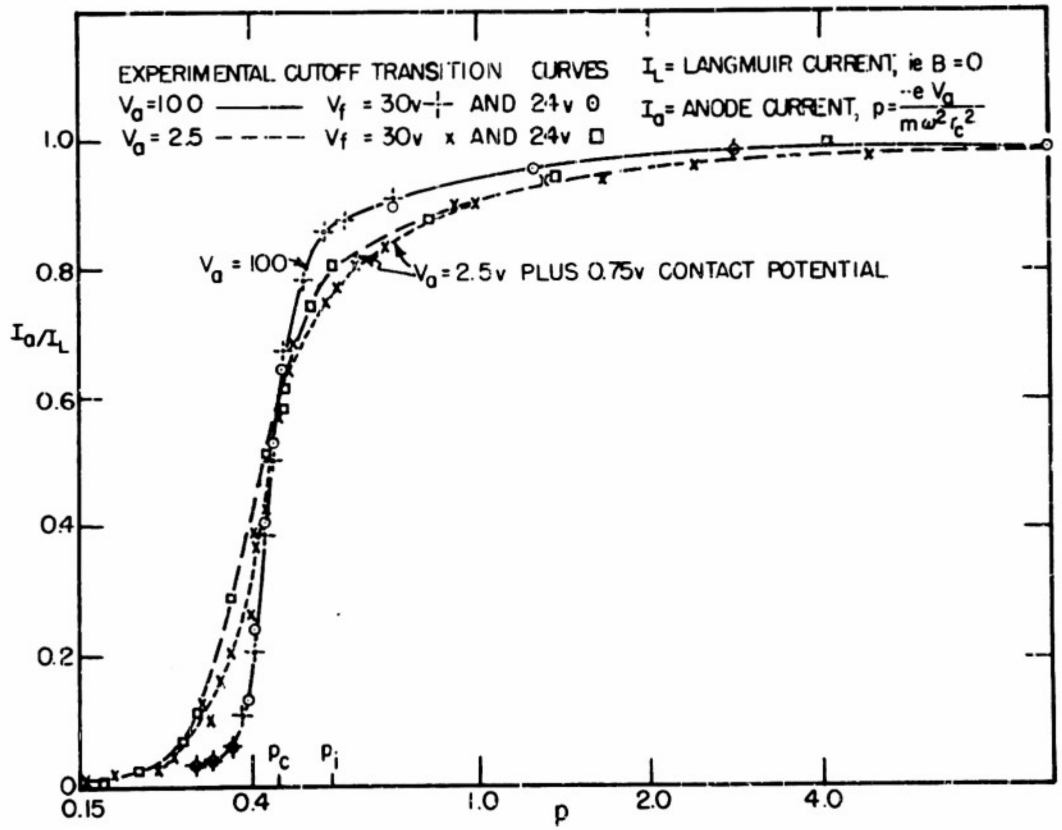

FIGURE 3-4

region on a, h and ψ'_c. The calculations carry us only to $\xi = 0.06$ or 0.02 cm from the physical cathode in our diode. The calculation for the case with magnetic field stops then between s_m and s_n, yet to carry it further without a consideration of trapping orbits and collisions seemed unrealistic. The assumption that all regions of W count twice, that the Hull radius is less than the anode radius, much simplifies the calculation for the cathode in a magnetic field. In the case without magnetic field one must distinguish single and double regions on the $(\bar{x},\bar{y})$-plane, so the integration starts at ψ_m, ξ_m and moves radially both outward and in toward the emitting surface.

To give a few details, we integrate Poisson's equation (2.21) with the initial conditions $\psi_c = 0$, and the set of six values of ψ'_c shown in Fig. 3-5 for h = 10, and five values of ψ'_c for h = 0. The values $a = 10$ and h = 10 are appropriate to our diode in a magnetic field after cutoff. Figure 3-5 shows solid curves of ψ and ψ' for h = 10, and dashed curves for h = 0.

Each solid curve was started by Wheatcroft's solution (2.24) and continued in this form until $S(\xi)$ fell appreciably from $\exp(-\psi)$, the value assumed in (2.24). The transition to a numerical method at $\xi = \xi_1$ actually occurs when, in each case, $\bar{y}_1$ as given in (3.4) equals 1.5. We find S is still greater than $0.95 \exp(-\psi)$ at ξ_1. From ξ_1 we carried the integration forward in steps $d\xi = \xi_i - \xi_{i-1}$, using (3.6) at each step to plot the boundary of W_i. To evaluate the integral of the distribution $\exp\left\{-(\bar{x}^2 + \bar{y}^2)\right\}$ we placed over each W_i a transparent sheet divided in 0.2 x 0.2 squares, each labelled according to its weight in the distribution. We then added up the weights of the squares within W, including fractional weights for squares cut by the boundary. The total was $S_i \exp(\psi_i)$. Conventional integration formulae then gave ψ'_i and ψ_i, which were used in turn to compute the boundary of W_{i+1}.

Figure 3-6 carries further the comparison of the solid and dashed curves. We see there, for given a and ψ'_c, that ξ_m occurs earlier and ψ_m is lower for h = 10 than for h = 0. Indeed, ψ_m and ξ_m, h = 0, are about the same for a given initial condition ψ'_c as ψ_m and ξ_m, h = 10, for $\psi'_c + 15$. The displacement, 15, in ψ'_c is due chiefly to our assumption that with h = 10 the magnetron diode current is cutoff, and that all parts of W have as many falling electrons as rising ones. Consequently the normalized charge density

S at an arbitrary point beyond ξ_m (actually the second zero of ψ) is nearly twice as large for a given ψ'_c when h is ten as it is when h is zero. The dashed lines in Fig. 3-6 represent $S_o(\psi'_c)$.

In integrating the dashed curves back from the virtual cathode to $\xi = 0$, we had to estimate the pairs of initial conditions $(\xi_m \psi_m)$ which would yield $a = 10$ at $\xi = 0$. These estimates resulted in slight deviations of a from 10. The deviations range from 0.02 for curve 1 in Fig. 3-5 to 0.10 for curve 5.

e. Review

Figure 3-7a shows clearly the bell-like shape of the distribution function $\exp\left\{-(x^2 + y^2)\right\}$. We have seen how the equations of the electronic orbit, (2.3) or (3.2), cut away the wings of this distribution. The boundary of the cut depends on the shape of the potential function, $\psi(s^*)$ or $\chi(s^*)$; indeed the $\overline{y}$-coordinates of points on the boundary are just the slopes of certain tangents and sectors shown in Fig. 3-7b. The sketch shows clearly the progression $y_3^2 > \overline{y}_1^2 > (y_2/s)^2 > \overline{y}_4^2/s_m$; and with $h^2 > 0$, the same progression in Y_i could be found on a curve $\chi(s^*)$.

In Chapters II and III we have concentrated on the cathode region. In Chapters IV and V we take a larger view and regard this region as a surface layer on the space between physical cathode and anode cylinders. As the source of electrons for the interval $s_n < s < s_a$, which we may call the interaction region, the cathode layer determines the number and velocity distribution of the electrons that enter the interaction region. In this sense a, h, and ψ'_c are independent parameters, but in another sense ψ'_c, ψ_m, s_m, s_n, and the other features of the surface layer depend on the anode voltage V_a, and on the distribution of space charge within the interaction region.

In the diode before cutoff, and even rather close to the cutoff transition, the Langmuir potential function (1.23, 2.32) gives $\psi(s^*)$ through the interaction region, for V_a positive and large enough. This function, fitted in the cathode layer to curve 2 of Fig. 3-5a, appears as ψ_L in Fig. 3-7c. The curves $\chi_L \equiv \psi_L + h^2(s-1)$ in this figure represent two cases: for h = 6.6, χ_{LI} corresponds to $p = p_i$ where thermal effects on the cutoff transition begin, and for h = 7.5, χ_{LC} corresponds to cutoff, $p = p_c$. The radii s_m and s_n are

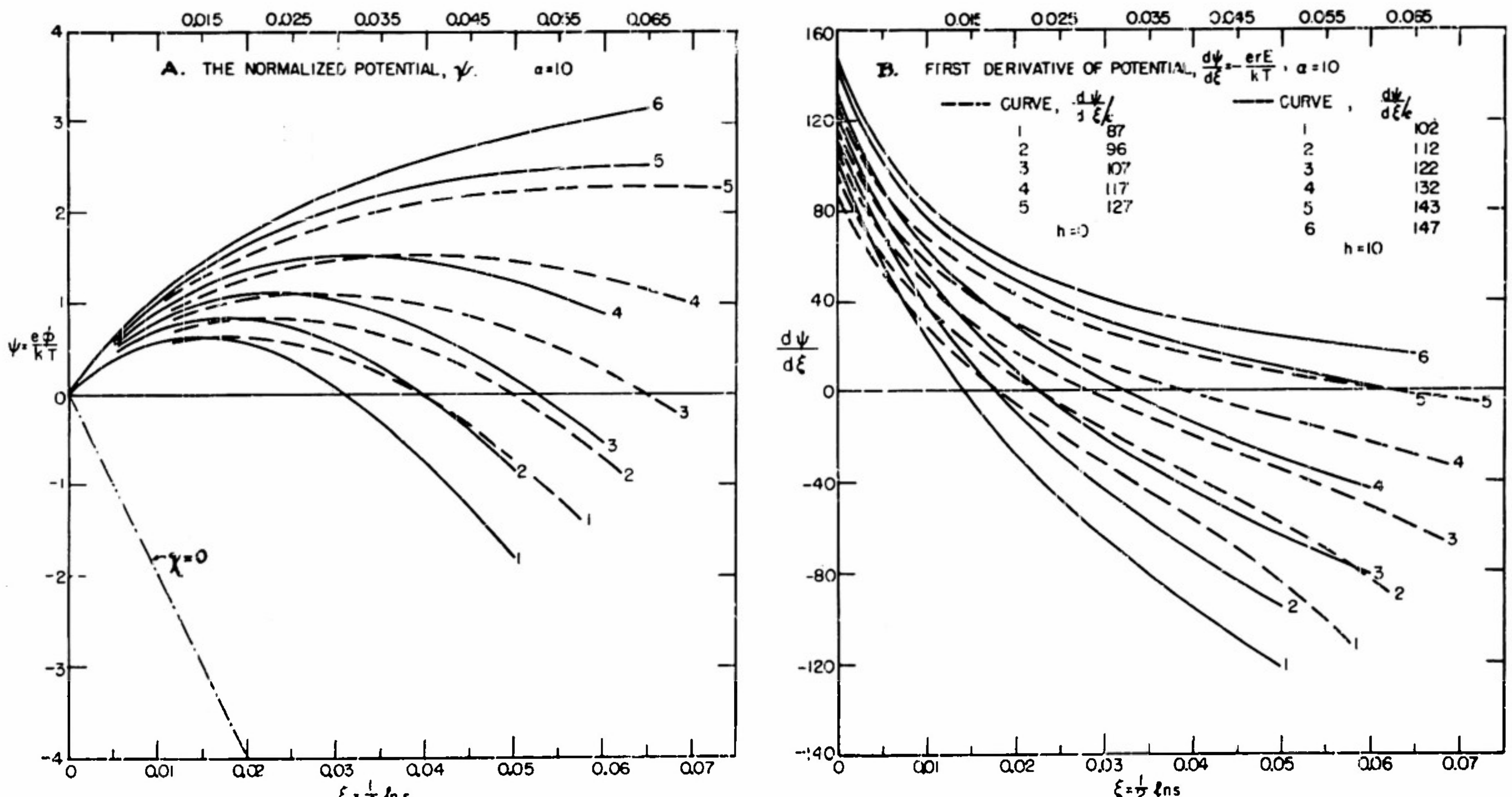

FIG. 3-5 EFFECTS OF AN AXIAL MAGNETIC FIELD ON POTENTIAL NEAR THE CATHODE SURFACE

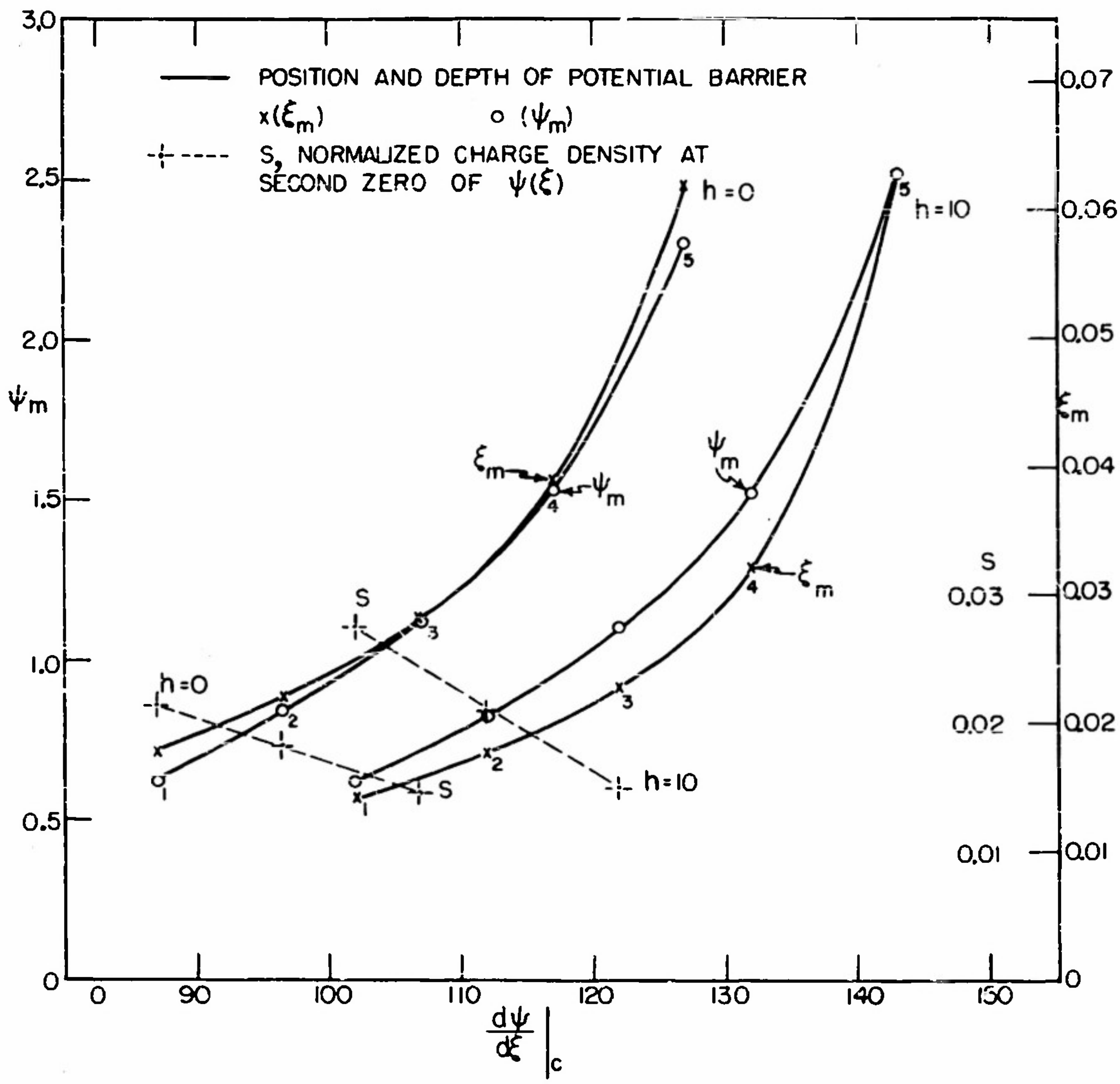

FIG. 3-6 COMPARISON OF CASES h = 0, h = 10, FOR SAME EMISSION, α = 10, AND VARIOUS ELECTRIC FIELDS AT THE CATHODE $\left(\frac{d\psi}{d\xi}\Big/_c = \psi_c'\right)$

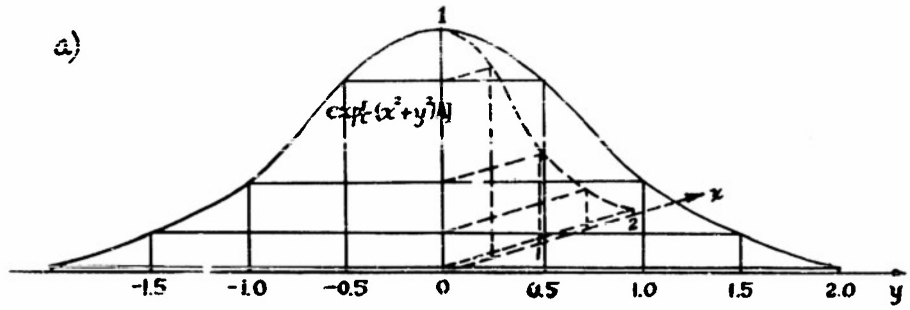

BELL-SHAPED MAXWELLIAN DISTRIBUTION FUNCTION

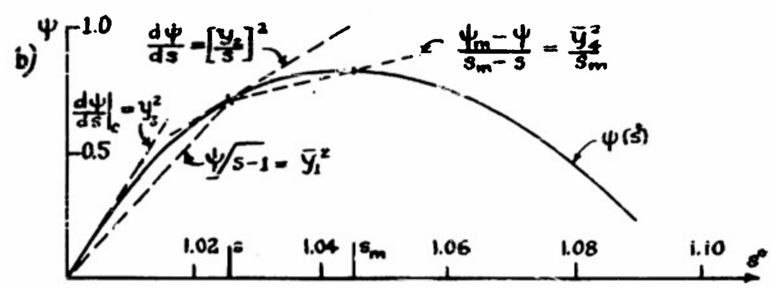

RELATIONS OF y_i TO SLOPES ON CURVE $\psi(s^*)$, $s_m > s > 1$.

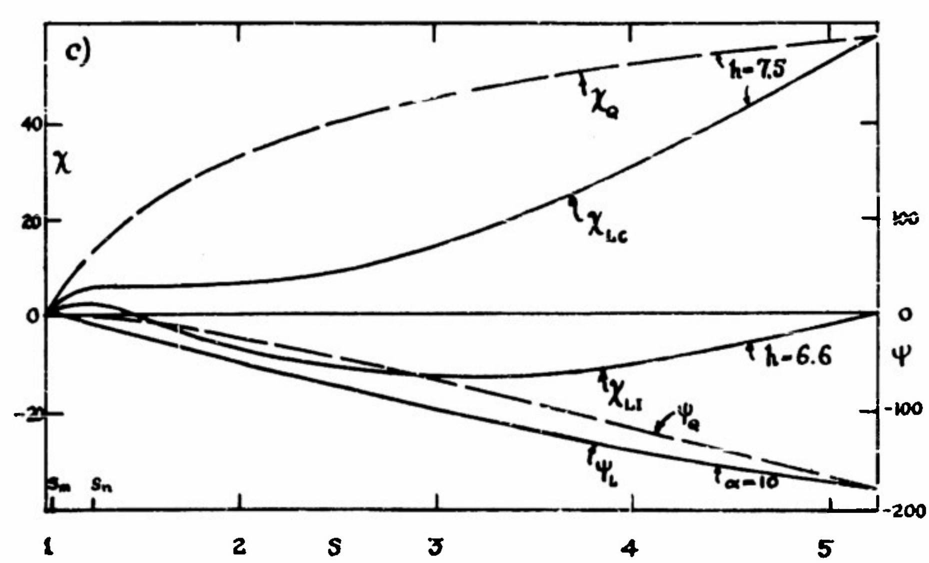

POTENTIALS $\psi(s)$ AND $\chi(s)$ JUST BEFORE CUTOFF, $p \geq p_c$.

FIG 3-7

indicated for χ_{LI}; this curve has a second maximum at s_a, a semicubic shape, and an inflection point between 1 and 2, although ρ, the charge density, does not vanish in this interval of s. One may also compare (1.13) of T.R. 185, the expression for u^2, with this expression for the inflection point:

$$\frac{d^2\chi_L}{ds^2} = \frac{d^2\psi_L}{ds^2} = \frac{er_c^4}{4r^2kT}\left[\frac{2E}{r} - \frac{\rho}{\epsilon_o}\right] = 0 \qquad (3.24)$$

The dashed curves in Fig. 3-7c represent a quadratic potential function ψ_Q and a corresponding χ_Q curve. At cutoff, the correct curve for χ is probably closer to χ_Q than to χ_{LC}, because of collision interactions. These, we will argue in Chapter V, provide a charge transport mechanism which seems to move the center of gravity of the whole charge cloud out away from the cathode layer.

References in Chapter III

1. G. Collins, Microwave Magnetrons, McGraw-Hill, New York, 1948, Vol. 6 of Rad. Lab. Series.

2. L. Marton, Editor, Advances in Electronics V, Academic Press, New York, 1953.

IV

The Magnetron Diode After Cutoff

a. Introduction

Most models for the distribution of space charge within a magnetron diode after cutoff provide at the Hull radius s_H an outer boundary for the charge cloud. In this chapter we consider three well known models of the bounded cloud. After a review of the probe signal evidence, we reject these models in favor of an "unbounded" cloud. We conclude that the space charge entirely fills the interaction space in the diode and formulate the potential function for this model.

b. Models of a Bounded Space Charge Cloud

Hull, as we noted, based his ideas in 1921 [1] on Langmuir's model of a cylindrical diode without magnetic field (1.35*; since formulae in T.R. 185 occur often in this chapter, we indicate references to that report by an asterisk). With the energy and momentum relations (1.4*, 2.1), Hull explained the sharp cutoff of anode current at the critical ratio p_c, of anode voltage V_a to the square of the magnetic field. If these relations apply in the same way after cutoff, if virtually all electrons within the space-charge cloud retain the energies and the canonical momenta that they have on leaving the cathode, then the cloud consists of electrons in emission orbits. Such a cloud will be bounded by a radius s_H equal to the outer turning radius s_b of the typical emission orbit.

The potential at $s_H = s_b$ (1.7*) in this case must pass smoothly into a logarithmic potential appropriate to the charge-free cylindrical region beyond s_b:

$$\Phi(s) \equiv -\frac{e\phi(r)}{m\omega^2 r_c^2}, \quad s \equiv \left(\frac{r}{r_c}\right)^2 \;;\; \Phi(s_H) = \frac{(s_b-1)^2}{8s_b} \quad . \tag{4.1}$$

$$\Phi(s) = \Phi(s_H) + K(s_H)\ln\left(\frac{s}{s_H}\right), \; s_H < s < s_a \;;\; K(s) \equiv \frac{d\Phi}{d\ln s} \quad . \tag{4.2}$$

If the quadratic expansion for potential (1.14*) represents the potential throughout the radial extent of the cloud, we have:

$$\Phi(s) = \left(\frac{s-1}{8s}\right)[B + C(s+1)] \;,\; K(s) = \frac{1}{8}\left[Cs + \frac{B+C}{s}\right], \; 1 < s < s_H \tag{4.3}$$

If the electric field in this case vanishes at the cathode, $K(1) = 0$, then with (4.1) we find the constants B and C: $C = 1$, $B = -2C$. The resulting potential, $\Phi(s) = \underline{(s-1)^2}/8s$, was proposed by Brillouin in 1941 [2] for the region within the cloud. It requires the canonical angular momentum P to equal one throughout the cloud; hence the circumferential velocity Y vanishes at the cathode, as it should if the average emission component is zero:

$$P \equiv \frac{2s}{\omega}\left[\dot\theta + \frac{\omega}{2}\right] = 1 \;;\; Y = \frac{2r\dot\theta}{\omega r_c} \;,\; Y(r_c) = 0 \quad . \tag{4.4}$$

Let us examine briefly Brillouin's famous model: Setting $1 - C = 0 = u^2$ implies the absence of radial motion. We note from (1.15*) that the state

$u^2 < 0$ is unstable, for if u^2 is negative, s becomes a hyperbolic function of time. Then the electrons soon hit a surface of the tube, or at least leave the region where u^2 is less than zero. Since u^2 represents in part the charge density (i.13*), a charge cloud with negative u^2 soon thins out until u^2 becomes positive. Brillouin's model lies at the edge of this unstable condition, and Brillouin's cloud has the maximum density permitted in a given magnetic field. Since in his model the electrons have no radial motion, they move around the cathode as a single slipping stream. He devotes much of his most recent paper on the magnetron [3] to showing how, as one slowly raises V_a from zero, a single cloud in such motion can form.

Brillouin there also states and proves a theorem that the double-stream model, a rival model proposed by Page and Adams in 1946 [4], is only possible for $\sqrt{s_H} \geq 2.273$. However, this theorem and both models depend on the assumption that the thermal distribution of emission velocities may be ignored. Twiss has shown [5] that this assumption and the uncritical use of Llewellyn's equation lead to singular rather than general results. Nothing significant in magnetron data occurs at 2.273.

Let us also examine the model of Page and Adams: In it the space charge consists of two equal and opposite radial currents, I_1 and $-I_1$, and also flows as one circumferential current around the cathode. The radial motion requires a potential to which the quadratic form (4.3) cannot come very close, but one can show that u^2 lies in the interval 0.15 to 0.075. Hence the charge density in this model is not very different from Brillouin's. The probe signal data includes values of u^2 from one to 0.25, but no values of u^2 were found closer to zero. Still, one must add, such resonances might be too broad to show up at all.

Twiss [5] recently described a multiple stream model, not too different from the model of Page and Adams. In his set of initial assumptions, however, he included a thermal distribution of emission velocities. In Chapter III this led us to define a release radius in a region of accelerating field. Disregarding other effects of emission velocities, we can easily include the electric field at the virtual cathode, K(1), as an adjustable parameter in the double stream model. Ignoring many elegant aspects of the treatment by

Twiss, we will develop this model in the rest of this section. The reasons we give for rejecting it will apply as well to his treatment.

To find u^2 in the modified double stream model, we define M (1.18) in terms of I_1, the outward component of radial current, and then develop a form like (1.19):

$$M \equiv eI_1 \, (2\pi h \epsilon_o m \omega^3 r_c^{\,2})^{-1} \; ; \tag{4.5}$$

$$\Phi(s) = K(1) \ln s + M \int_1^s \frac{(\ln s - \ln s^*)\, ds^*}{\sqrt{8s^* \Phi(s^*) - (s^*-1)^2}} \, , \quad 1 < s < s_H \, . \tag{4.6}$$

We may develop $\Phi(s)$ as a function of the parameters K, M and s_H, by iteration over the charge-free potential $\Phi_o(s^*)$, and express M and K in terms of s_H (or s_b) and a new parameter $\overline{m}$:

$$\Phi_o \equiv \frac{\Phi(s_H) \ln s^*}{\ln s_H} \; , \qquad K(1) = \frac{(1-\overline{m})\Phi(s_H)}{\ln s_H} \; ; \tag{4.7}$$

$$\overline{m} \equiv \frac{M}{\Phi(s_H)} \int_1^{s_H} \frac{(\ln s - \ln s^*)\, ds^*}{\sqrt{8s^* \Phi(s^*) - (s^*-1)^2}} \; . \tag{4.8}$$

Here $\Phi(s_H)$ is given in (4.1), and we extend $\Phi(s)$ in the interval $s_H < s < s_a$ with (4.2). Thus we find $p(\overline{m}, s_b) \equiv \Phi(s_a)$. Knowing $\Phi(s)$, we may also evaluate $u^2(\overline{m}, s_b)$:

$$\theta_b = \int_1^{s_b} \frac{ds}{\sqrt{8s\Phi(s) - (s-1)^2}} = \omega T_b = \pi u \tag{4.9}$$

In Fig. 4-1a we plot the inverse relations, contours of $\overline{m}$ and k on the (p, u^2)-plane. The quantity $\overline{m}$ represents the field at the cathode; thus if K(1) = 0, $\overline{m}$ = 1, and if $\overline{m}$ = 0 then K(1), for a given p, has its maximum, a value appropriate to the cathode field in a charge-free coaxial region. The quantity k represents the radial extent of the cloud of charge:

$$k \equiv \frac{s_b - 1}{s_b + 1} \doteq \frac{r_b}{r_c} - 1 \tag{4.10}$$

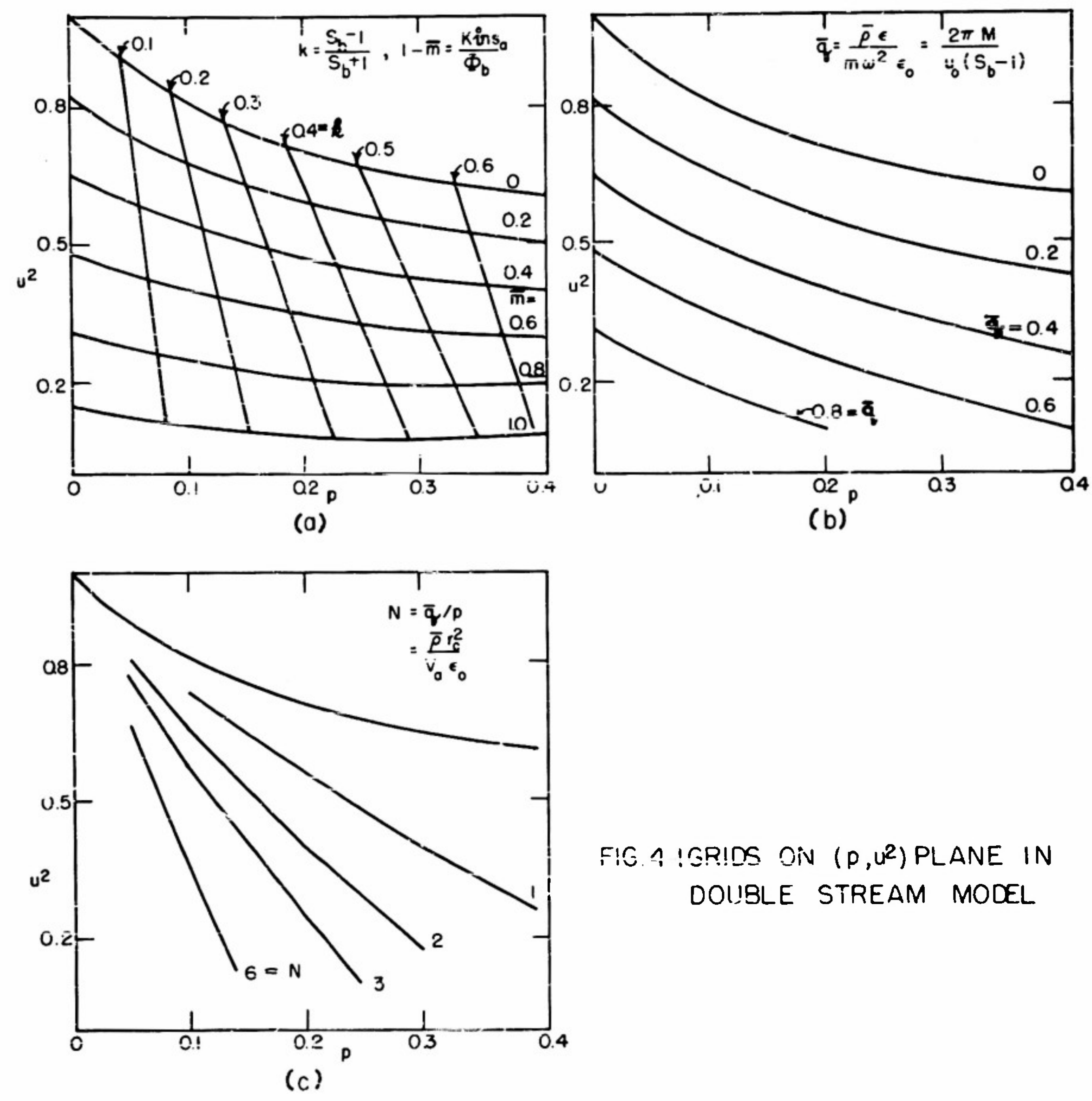

FIG. 4 GRIDS ON (p, u^2) PLANE IN DOUBLE STREAM MODEL

Although we made only one iteration over Φ_o for the $\Phi(s)$ used in the $(\overline{m},k)$-grid, we believe from results of a direct calculation for a planar diode that further iterations would not change this grid much. The absorption data of Fig. 4-2*, interpreted with the grid on Fig. 4-1a, imply very high values of K(1) as p approaches zero. The data do not suggest the line $K(1) = E_c = 0$, $\overline{m} = 1$, appropriate to the Page and Adams model.

The parameter $\overline{m}$ (or M) also gives the charge density ρ in the cloud (1.18, $M = \rho e s/4m\epsilon\,\omega^3$). Introducing the symbol $\overline{q}$ for the average (barred) space-charge density inside s_H, we write:

$$\overline{q} = \frac{\overline{\rho} e}{m\epsilon_o\,\omega^2} = 4M\omega\left\{\overline{\frac{1}{s}}\right\} = \frac{4M\omega}{s_H - 1}\cdot\int_1^{s_H}\frac{ds}{s} = \frac{4\pi M}{(s_H-1)u} \quad . \tag{4.11}$$

From this one obtains the $\overline{q}$-grid on the (p,u^2)-plane, Fig. 4-1b. The absorption data do not fall along any contour of average charge density normalized with respect to ω^2. However, dividing $\overline{q}$ by p serves to renormalize $\overline{\rho}$, with respect now to V_a. This yields the contours $N = \overline{q}/p = \overline{\rho} r_c^2/V_a\epsilon_o$ in Fig. 4-1c. The absorption data tend to follow the line N = 1.5. This suggests that the anode voltage determines $\overline{\rho}$, and actually led us to try the quite different model described below.

c. Evidence for an Unbounded Charge Cloud

We have seen that modifying the double stream model to include a finite electric field at the cathode is not enough to interpret the probe signal data. Let us then consider relaxing the energy condition. We noted that the charge cloud is bounded by s_H in any model in which individual interactions do not disturb the electronic orbits. We saw that s_H must retreat toward the cathode as p falls from p_c toward zero. However, if interactions do permit electrons to exchange energy and momentum at a significant rate, then the space-charge cloud may extend to the anode for all values of p. Hull apparently had such a model in mind in 1924 when in an abstract [6] he suggested that the cloud formed "a solid shaft of rotating electricity."

There is little experimental evidence for a well-defined outer boundary to the charge cloud. Reverdin [7] four years ago passed a wide beam of electrons parallel to the polar axis through a grid, the magnetron diode and a second grid. On a phosphor screen he observed the beam, the shadow cast by these grids, and the distortion in these shadows due to the beam's having passed through the radial field in the magnetron cloud. He found at first indications of a maximum density near s_H, but as he brought his cathode into alignment with the beam and the magnetic field, the density became a smooth decreasing function of radius. Peterson [8] this past year passed a very narrow electron beam axially through the magnetron cloud, observed its deflection, and concluded there was considerable charge outside the nominal Hull radius. Knoll and Nedderman [9] have used excited helium atoms to indicate the space-charge distribution. They found "as the anode voltage is lowered, the charge density decreases, and the position of maximum density shifts toward the anode."

Several experiments have detected electrons which gained great energy within the interaction space and were not, therefore, in emission orbits. For example, we recall the experiments on cathode heating by back bombardment [10]. Wigdortschik [11] and Linder [12], as further examples, measured currents to "hats" at the ends of the diode axis when these hats were much more negative than the cathode, hundreds of volts move negative when the anode was over a thousand volts positive.

Moreover, the electrons collected as leakage current at the anode are not in emission orbits. As p falls, the anode current I_a continues to flow; and in any bounded cloud model, we must, it would seem, imagine a mechanism that knocks some electrons out of the cloud and clear to the anode, yet does not fill the stable orbits that lie like traps between s_H and s_a. The curves in the four square sections of Fig. 4-2 show I_a over a range of p after cutoff. Each section gives data for a fixed V_a, and within each section the cathode temperature T_c is a parameter. The coordinates, p and I_a/I_L, used before in Fig. 3-4, here are plotted on logarithmic scales. The same contact potential, 0.75 volts, was added to V_a in computing p. The cutoff transition lies roughly above p = 0.4. I_a/I_L comes out of a vertical dive about at 0.04, and after cutoff depends not only on p, but also on V_a and T_c. The dependence on T_c may in part reflect changes in gas pressure in the (sealed off) tube.

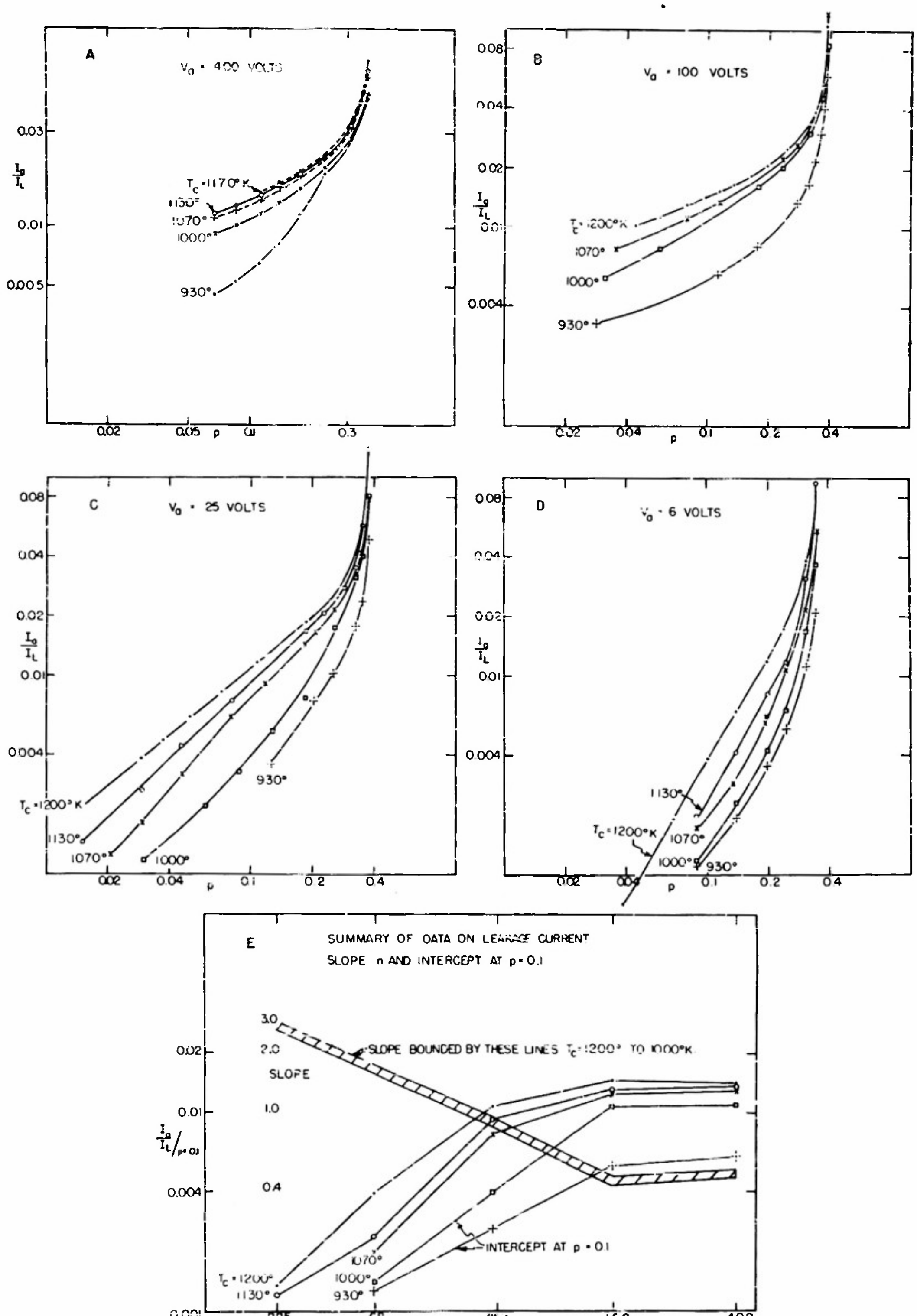

FIG. 4-2 LEAKAGE CURRENT AFTER CUTOFF

Figure 4-2e compares the data in the four sections above it. The slope $d \ln(I_a/I_L)/d \ln p$ is nearly independent of T_c and decreases as V_a rises, while the intercepts of the current curves at p = 0.1 increase with V_a and with T_c.

For p below 0.1 some curves of leakage current (Fig. 4-3) show "humps." Such humps appeared in the first published cutoff curves (Fig. 11 of Hull's paper [1]) and have reappeared in subsequent articles. The hump for V_a = 1.5 in Fig. 4-3 is not affected by T_c, but the hump for V_a = 6 volts seems to move toward lower values of p as T_c falls. We have described a drag-loop effect of the probe signal within one such hump (Fig. 4-5b*). These humps do not, in our tube, produce strong noise or oscillations, and they occur only well removed from cutoff.

Thus in summary, if electrons in orbits of the emission type are the exceptional ones, if the average electron suffers many collisions or a continual exchange of energy and momentum with its neighbors during its life-time in the cloud, one would not expect the cloud to have a sharp edge at s_H. Although the anode current drops sharply in the cutoff transition, indeed from 80 to 3 per cent of the Langmuir current, I_a continues to flow for very low values of p. We find little support for the suggestion that the diode after cutoff maintains an electron cloud bounded by a contracting radius s_H, a radius as sharply defined as the cutoff transition is.

d. The Potential in an Unbounded Cloud

We found in T.R. 185 a reasonably sharp and deep resonance absorption over most of the interval $0 < p < 0.3$ (Fig. 4-2b*). We would have seen multiple resonances, perhaps smeared into a broad region of absorption, if distinct values of u^2 were characteristic of different radial intervals within the space-charge cloud. Hence one value of $u^2 = 1 - C$, for a given set of conditions p, λ_p and T_c, must characterize at least roughly the whole interaction space, if the cloud extends practically to the anode after cutoff. If we accept a two-parameter potential function, and one parameter applies in the whole radial interval $1 < s < s_a$, then the other must also apply throughout this interval, if the potential $\Phi(s)$ is continuous in s. The two parameters could be B and C (4.3), but the potential may now be completely determined by two measurable quantities, u^2 and p/p_c:

$$B = \frac{p}{p_c}(s_a - 1) - (1 - u^2)(s_a + 1) \quad , \quad C = 1 - u^2 \quad ; \tag{4.12}$$

$$\Phi(s) = \frac{s-1}{8s}\left[\frac{p}{p_c}(s_a - 1) - (1 - u^2)(s_a - s)\right] = -\frac{e\phi}{m\omega^2 r_c^2} \quad ; \tag{4.13}$$

$$K(s) = \frac{1}{8s}\left[\frac{p}{p_c}(s_a - 1) - (1 - u^2)(s_a - s^2)\right] = \frac{erE}{2m\omega^2 r_c^2} \quad ; \tag{4.14}$$

$$\frac{q(s)}{4} = -\frac{1}{8s^2}\left[\frac{p}{p_c}(s_a - 1) - (1 - u^2)(s_a + s^2)\right] = \frac{e\rho}{4m\omega^2\epsilon_o} \quad . \tag{4.15}$$

We found in Fig. 4-2* that most resonance data fall near the line $1 - u^2 = p/p_c$. If this relation is added to (4.12) then $2C + B = 0$, and the next three quantities are:

$$\Phi(s) = \frac{p}{8sp_c}(s-1)^2 \; , \quad K(s) = \frac{p}{8sp_c}(s^2 - 1) \; , \quad \frac{q(s)}{4} = \frac{p}{8p_c}\left(1 + \frac{1}{s^2}\right) \tag{4.16}$$

At cutoff, $p = p_c$, these formulae are the same as those derived from Brillouin's model. The formula for q(s) in (4.16) was first used in (2.44*). For all values of p, K(1) = 0, and the electric field in (4.16) vanishes at the cathode. We regard as a partial confirmation of our model of an unbounded cloud the fact that K(1) = 0 arises from this interpretation of resonance data.

In Fig. 4-2* points (p,u^2) numbered 1 and 2 were singled out to represent the resonance absorption in our magnetron diode with a hot cathode. Figure 4-4a shows potential curves corresponding to these points; the solid curves are based on (4.13) and the dashed curves on Brillouin's model. In each case $8s\Phi$ is plotted against s. Clearly the Brillouin potential, or indeed any potential based on a cloud bounded by s_H, lies well above the corresponding solid curve for $s > s_H$.

In Fig. 4-4b the solid curves are the standard ones for a diode without magnetic field, the Langmuir and the logarithmic (space-charge free) potentials. The dashed curves reproduce the solid curves of Fig. 4-4a, but the ordinate has been renormalized as $s\Phi/s_a\Phi_a$ to make a comparison of curve

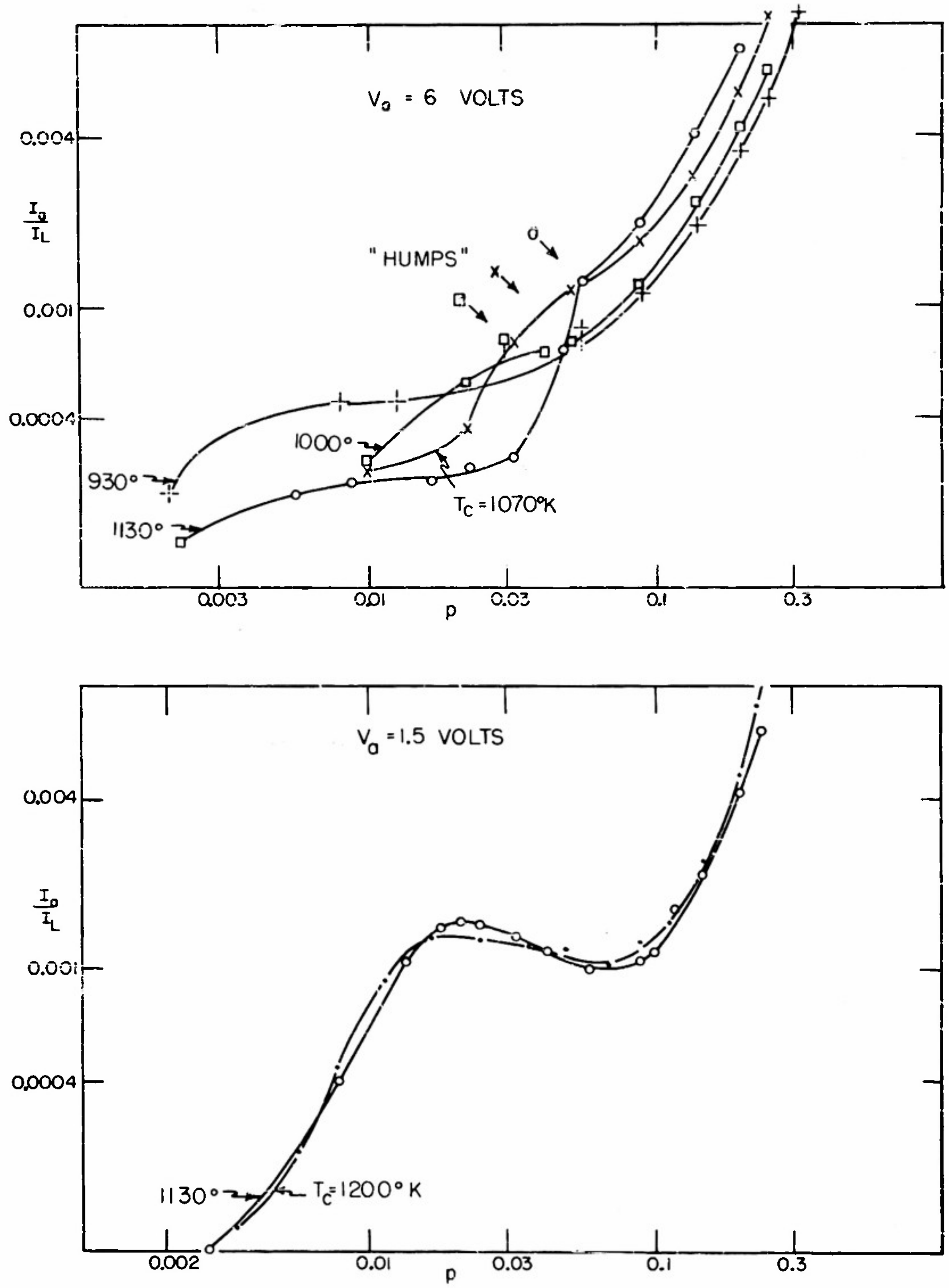

FIG. 4-3 REMOTE LEAKAGE CURRENT

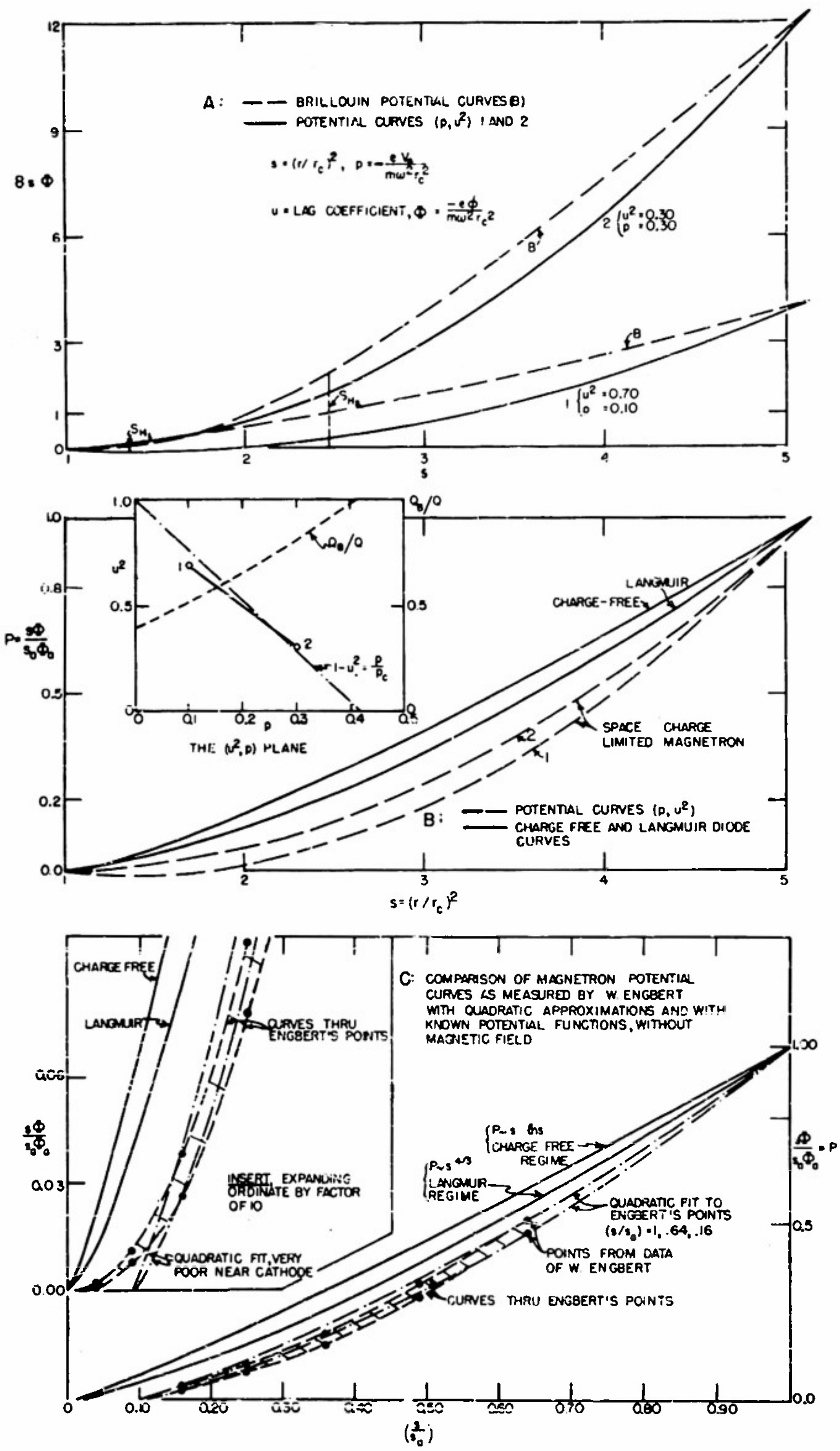

FIG. 4-4 REPRESENTATIVE POTENTIAL FUNCTIONS

shape easier. Again the potential curves based on (4.13) lie below the standard curves.

The insert in Fig. 4-4b shows the dot-dash line $1 - u^2 = p/p_c$ and the representative points, 1 and 2, lying very close to this line on the (p,u^2)-plane. The dashed line Q_B/Q compares the Brillouin model and the unbounded model (4.16) with respect to total charge inside the cloud as a function of p. Clearly the cloud extending to the anode admits more charge than the Brillouin cloud bounded by s_H:

$$Q(s) = \frac{e \cdot 2\pi h}{4m\omega^2 \epsilon_o} \int_1^s \rho ds = 2\pi h\,[K(s) - K(1)]$$

$$\frac{Q_B}{Q(s_a)} = \frac{s_H+1}{s_a+1} \cdot \frac{s_a-1}{s_H-1} \cdot \left\{1 + \frac{s_H+1}{s_H-1} \ln \frac{s_a}{s_H}\right\}^{-1} \tag{4.17}$$

$$Q_B: B = -2 \, , C = 1 \, , \quad 1 < s < s_H; \; Q(s_a): B = -\frac{2p}{p_c} \, , C = \frac{p}{p_c} \, , \; 1 < s < s_a .$$

Figure 4-4c represents potentials in a diode with a very large ratio of anode to cathode radius, s_a. W. Engbert in 1938 [13] used such a diode, with filamentary cathode of about 0.2 mm radius and anode of 7 mm radius, in experimental measurements of the radial variation of potential in a magnetron after cutoff. His measurements, the only ones so far reported, deserve more consideration than they seem to have received. The points ⊙ in Fig. 4-4c are replotted in coordinates $(s/s_a, s\Phi/s_a\Phi_a)$ from Engbert, Abbild 5, and the solid curves again represent the Langmuir and logarithmic potentials. The dashed curves through the points ⊙ have much the same relation to the solid curves as the dashed curves 1,2 have to the same solid standard curves in Fig. 4-4b. In particular, the dashed curves lie well below the solid curves near the anode and indicate a denser space charge near the anode. Engbert's data lend no support to the models that confine the charge cloud inside a radius $s_H < s_a$.

Two figures reproduced from Engbert's paper appear in Fig. 4-5. Abbild 2 shows his smooth anode tube suspended between magnet faces M with cylindrical axis vertical. He could move a fine tungsten wire radially through the interaction space. At the end of this wire he attached a sliver of tungsten (A). The potential V_s, applied to the wire by the potentiometer circuit shown in Abbild 1, would deflect the sliver toward anode or cathode. When opening and closing switch T did not deflect the sliver from the vertical, Engbert recorded V_s as the undisturbed potential in the diode at the radial position r_p of the sliver. Through a microscope trained on a slit in the anode he observed the sliver by the light of the hot tungsten cathode. If V_a was larger than 150 volts, he felt he could determine V_s more accurately than r_p. Without a magnetic field he obtained data for good curves of the standard Langmuir and logarithmic potentials.

After the magnetic field cut off the anode current, he reports, the strength of the field and the cathode temperature T_c had, within wide limits, no effects on the potential distribution. (His experimental points actually have the spread indicated in Fig. 4-4c, so it seems likely that within this spread one might find correlation between $\phi(r_p)/\phi(r_a)$ and V_a and T_c.) He examined a wide range of T_c, but he does not give the range of p he examined.

Engbert's interpretation of his results is a little forced. He approximated his potential by two straight lines, meeting at r_o, the radius that gave the best fit to his data:

$$V(r) = 0, \; r_c < r < r_o \; ; \; V(r) = \frac{V_a(r-r_o)}{r_a - r_o}, \; r_o < r < r_a . \quad (4.18)$$

In the first interval he seems to believe there is no radial motion of electrons; in the second he draws electronic orbits like those proposed by Hull [1]. Doehler [14] fits Engbert's data with a curve $\phi(r) = V_a(r/r_a)^n$, $n = 0.875$. Twiss, (5, page 282) referring to these two types of fit, says "The accuracy of the measurements cannot be very high, if they are open to two quite different interpretations." Perhaps one might question first the accuracy of the interpretations.

For the present argument it is unfortunate that Engbert used a filamentary cathode. The enlarged corner section in Fig. 4-4c shows how

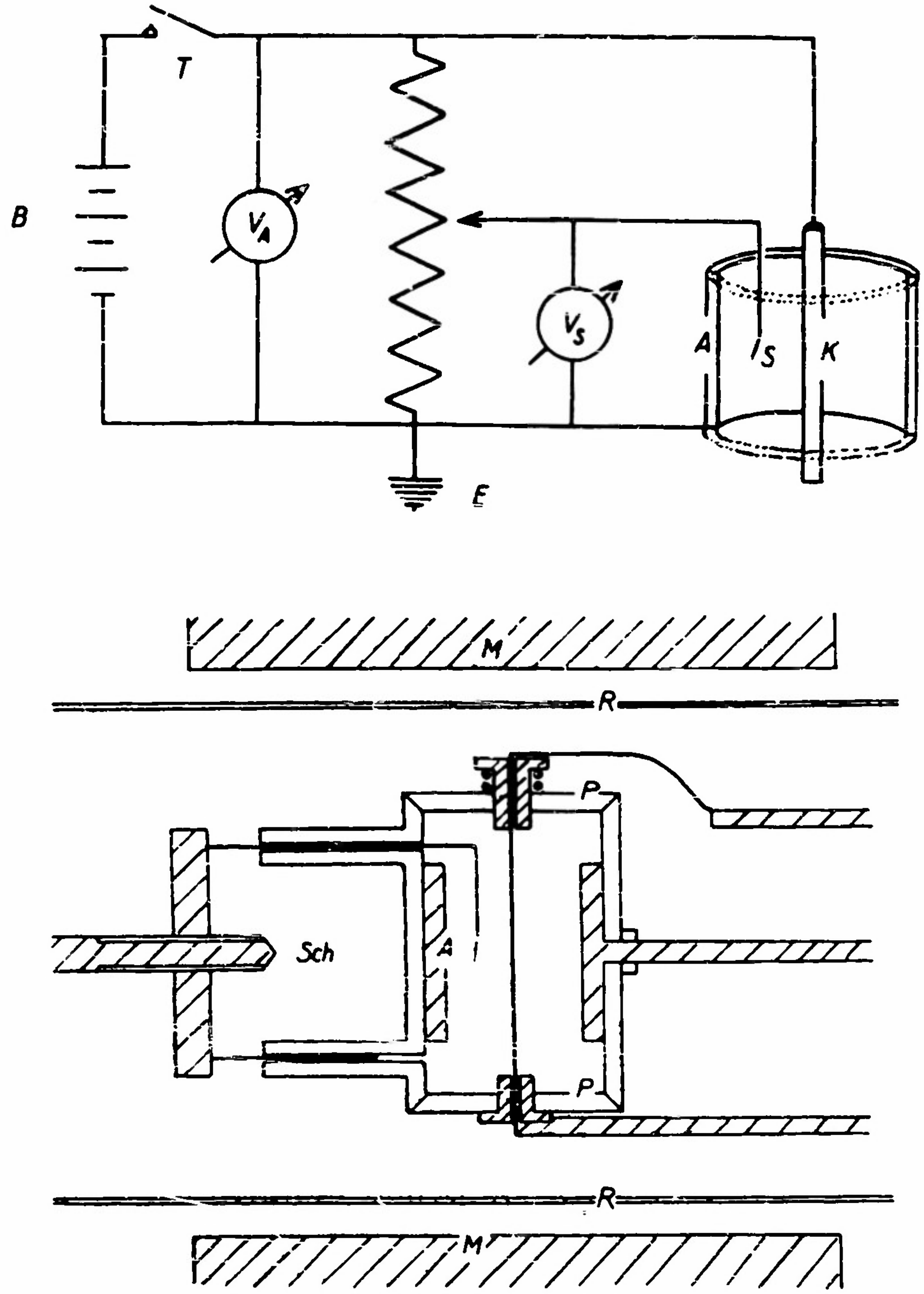

FIG. 4-5 ENGBERT'S EXPERIMENT
(HOCH FREQUENZ TECHNIK 51, 44-52 (1938))

poorly near the cathode a quadratic potential function (dot-dash curves) matches the potential he measured. Perhaps measurements like his, but made on a diode with a large cathode, would yield a potential function to which one could fit a quadratic form closely. The reciprocal inference, that a probe signal resonance in a magnetron diode with a filamentary cathode would be broad, must be drawn from Engbert's data. If the potential curve has a wide range of curvature, when plotted as in Fig. 4-4c, then as we noted above, the individual electronic orbits will tune to a range of frequencies. We have checked this inference: a pre-war model split-anode magnetron was mounted so as to transmit a TEM signal along its filamentary cathode. In it the cyclotron resonance absorption was observable but extremely broad. This was also true of the region in which a strong probe signal tended to reduce the anode leakage current.

In summary, then, we have developed a potential function for an unbounded space-charge cloud in a magnetron diode after cutoff. This function interprets well the normal resonance absorption data, and the radial electric field derived from it vanishes at the cathode. The unbounded cloud contains in fact more total space charge than the saturated clouds in models bounded by s_H. The cloud density is a function of anode voltage (p/p_c) and is always less than the saturated density, $q = \frac{1}{2}(1 + s^{-2})$. The potential function has a family resemblance to the potential Engbert measured in a magnetron diode with much larger s_a.

References in Chapter IV

1. A.W. Hull, "The Effect of a Uniform Magnetic Field on the Motion of Electrons between Coaxial Cylinders," Phys. Rev. 18, 31-57 (1921).

2. L. Brillouin, "Theory of the Magnetron I" Phys. Rev. 60, 385-396 (1941).

3. Bloch and Brillouin, "Electronic Theory of the Cylindrical Magnetron," p. 145 to 166 in Advances in Electronics III, L. Marton Editor, Academic Press, New York, 1951.

4. Page and Adams, "Space Charge in Cylindrical Magnetron," Phys. Rev. 69, 494-500 (1946).

5. R.Q. Twiss, "On the Steady State Theory of the Magnetron," in Advances in Electronics V, L. Marton Editor, Academic Press, New York, 1953.

6. A.W. Hull, Abstract, "The Paths of Electrons in the Magnetron," Phys. Rev. 23, 112A (1924).

7. D. L. Reverdin, "Electron-Optical Exploration of Space Charge in a Cutoff Magnetron," J. Appl. Phys. 22, 257-62 (1951).

8. W.W. Peterson, The Trajectron, T. R. 18, 1954, University of Michigan.

9. Knoll and Nedderman, Quarterly Report, Columbia, Department of Physics, New York, August 31, 1953.

10. R. L. Jepsen, Enhanced Emission from Magnetron Cathodes, Columbia University, May 1951.

11. I.M. Wigdortschik "The Velocity Distribution of the Electrons under the Influence of a Magnetic Field in a High Vacuum," Phys. Z. Sov. Union 10, 245-250 (1936).

12. E.G. Linder, "Excess-Energy Electrons and Electron Motion in High-Vacuum Tubes," Proc. I.R.E. 26, 346-371 (1936).

13. W. Engbert, "On the Potential Distribution in the Magnetron," Z. Hochfrequenztechnik, 51, 44-52 (1938).

14. O. Doehler, "On the Properties of Tubes in Constant Magnetic Fields," Ann Radioelectricite 3, 29-39, 169-183 (1948).

V

The Distribution of Electrons in Phase Space

a. Introduction

In this chapter we extend somewhat the statistical approach of Hok [1] to the problem of charge distribution within a magnetron after cutoff, and consider the density distribution f of electrons in phase space. One should, if possible, derive f as a solution of the Boltzmann transport equation (2, page 46), but this would require one to determine the cumulative effects of the individual interactions of electrons. Without attempting that difficult task, we present here in brief outline some features of these interactions and some conditions on the function f.

b. Individual Electronic Interactions

If two electrons of charge e in a cloud of particles approach each other so closely that one third of their average kinetic energy changes into potential energy of their mutual repulsion, they are then a distance $\underline{d}$ apart:

$$\frac{kT}{2} = \frac{e^2}{4\pi\epsilon_o d} \tag{5.1}$$

Since the electronic cross section for collisions of this type is $\pi d^2/4$, this $\underline{d}$ is a kind of electron diameter. The mean free path h between such collisions is $h = (n\pi d^2)^{-1}$, if $\underline{n}$ is the number density of electrons in the cloud.

Attempts at refining this crude picture of electronic interactions founder on the long range of the coulomb force, which tends to arrange all the charged particles in the cloud in a sort of lattice. If a section of this lattice is disturbed, it may interact as a whole with the electromagnetic field in which it lies, and this collective behavior may have a characteristic angular frequency, ω_b.

Individual particles jostle about within the lattice near centers of minimum energy in a somewhat random fashion. They may have a distribution $n_o \exp\{-e\phi/kT\} \doteq n_o [1 - e\phi/kT]$, where $\phi(r)$ depends on the distance $\underline{r}$ from such a lattice point. For a similar model of ions in a weakly ionized solution, Debye [3] derived the equation for $\phi(r)$:

$$\nabla^2\phi = \frac{1}{r^2}\frac{d}{dr}\left(r^2\frac{d\phi}{dr}\right) = -\frac{\rho}{\epsilon_o} = \frac{e^2\phi n_o}{kT\epsilon_o} = \frac{\phi}{\lambda_d^2} \tag{5.2}$$

The radius λ_d that arises in (5.2) is called the Debye screening radius. It is the geometric mean of the free path and the electron radius derived from (5.1): $\lambda_d^2 = \frac{dh}{2}$. The solution of (5.2) is:

$$\phi(r) = \frac{e}{4\pi\epsilon_o r} \cdot \exp\left\{\frac{-r}{\lambda_d}\right\} \tag{5.3}$$

A weak solution of ions has no net charge and consists largely of neutral particles that act as a heat bath. Despite such differences between Debye's model and an electron cloud, Bohm and Pines [4] find that

λ_d is a convenient distance to divide the interaction range within the cloud. Particles which come closer together than the distance λ_d, they claim, interact in a random individual manner, while particles further apart than this distance recognize only the collective motions of the entire lattice. The angular frequency ω_b they identify with the plasma frequency,

$$\omega_b^2 = \frac{e^2 n}{m\epsilon_o} .$$

For an example, let us set e/kT = 10 volts^{-1} and set the cyclotron frequency $\omega = 0.93 \times 10^{10}$ radians per second. Then we have $\lambda_d^2 = -.65 \times 10^{-10}$ (p_c/p) square meters, $h = 1.46 \times 10^{-3}$ (p_c/p) meters and $d = 0.89 \times 10^{-7}$ meters. Moreover, $\omega_b^2 \leq \omega^2(p/p_c)$, if from (4.16) we have

$$\frac{ne^2}{m\epsilon_o\omega^2} = \frac{p}{2p_c}(1 + \frac{1}{s^2}) .$$

We have seen no evidence of a plasma resonance in our absorption data, but one might expect to find it in response to an axial electric probe field, (3.44*). It would be quite distinct from the cyclotron type of resonance, $\omega_o^2 = \omega^2(1 - p/p_c)$, (4.3*).

c. General Conditions on the Distribution

Individual interactions may make the electrons in emission orbits the exceptional ones in the space-charge cloud, and require a statistical treatment. The statistical model proposed by Hok [1] is as extreme in this direction as the single and double stream models are in another direction. If the cathode and anode and the ends of the magnetron diode were reflecting walls, instead of source and sink for electrons, then the charge cloud, he points out, would fill the space between these walls, and the particles in it would, after many collisions, approach a thermal equilibrium. The spacial region of lowest potential $e\phi$ (since $\underline{e}$ is negative), would be close to the anode; and it would be the region of highest density, if $\underline{f}$ were proportional to the Boltzmann factor

$$\exp\left\{-\left(\frac{mv^2}{2} + e\phi\right)(kT)^{-1}\right\} .$$

We develop a less extreme form $\underline{f}$, which may range over all elements of a six-dimensional phase space $(\bar{x},\bar{y},\bar{z};\ r,\theta,z)$. Here we use $\bar{x},\bar{y}$ and $\bar{z} = \dot{z}\sqrt{\frac{m}{2kT}}$ as in (2.2). Of course, $\underline{f}$ is larger than zero only within the cylindrical interaction region in the diode, $r_c < r < r_a$, and $0 < z < h$. In the velocity subspace $(\bar{x},\bar{y},\bar{z})$, some regions imply orbits which collide with a physical boundary, and $\underline{f}$ should reflect a thin or one shot population in these regions. Another region of $(\bar{x},\bar{y},\bar{z})$ includes emission orbits and may have a denser population even though such orbits carry a small proportion of the particles in the space charge.

Since the leakage current and the probe signal data show for low V_a a dependence on the cathode temperature T_c, and a dependence on V_a that remains after normalizing V_a with respect to ω, we may expect f to depend on T_c and on V_a as well as on p/p_c. The first moment of $\underline{f}$, the charge density ρ, will with $\phi(r)$ satisfy Poisson's equation (1.16), and the radial velocity moment of $\underline{f}$ will give the anode current I_a:

$$\frac{\rho(r)}{\epsilon} = \frac{e}{\epsilon}\iiint_G f\, d\bar{x}\, d\bar{y}\, d\bar{z} \doteq \frac{m\omega^2}{2e}\left(1 + \frac{1}{s^2}\right)\frac{p}{p_c}. \tag{5.4}$$

$$I_a = 2\pi h\, r_c \mathcal{N}s\, e \iiint_G \bar{x} f\, d\bar{x}\, d\bar{y}\, d\bar{z}\sqrt{\frac{2kT}{m}}. \tag{5.5}$$

The domain G of these integrals is the domain of six-space within which $\underline{f}$ is greater than zero. We have noted above its spacial boundaries; we may assume now that $\underline{f}$ is independent of the polar angle θ. The motion of electrons along the z-axis maybe aperiodic and limited within G only by collisions. We assume, except close to the diode ends in small regions which we ignore, that $\underline{f}$ is independent of z. (For large values of $\bar{z}$, this may also be untrue.)

If details of the cumulative interaction processes were known, one might calculate the rate of transport of electrons from emission orbits through intermediate orbits to collection orbits. The over-all rate $\mathcal{T}/T$ is indicated in Fig. 4.3*. In general the electrons are knocked out of emission orbits at the rate required to replace those lost to the cloud through collection orbits, since the net radial leakage current is independent of time and of the radial coordinate. The more efficient the knocking out process, when compared to the radial transport mechanism effective throughout the cloud, the fewer electrons are required to complete emission orbits. In other words, the feature of the cathode region which most affects the interaction space, namely the barrier at the release radius, will be of such a height as to limit properly the number of electrons which leave the cathode region and follow emission orbits out through the interaction region.

To fix the boundaries of G in the subspace $(\bar{x},\bar{y})$ we must know the potential function $\Phi(s)$. We used a quadratic form for $\Phi(s)$, first in Chapter I* of T.R. 185 to approximate the potential over the radial extent of a single orbit, and more recently in Chapter IV of this report to represent the potential over the whole radial interval from cathode to anode. Clearly this quadratic form fails to represent the cathode region correctly, but the lack of multiple resonances in probe signal data and the high values of Q_s justify using the form in this chapter, too. These high Q_s values also indicate that electronic orbits of some stability are typical of the charge cloud. Hence, although we know little of the interactions which add up to determine f, we assume they are neither so strong nor so frequent as to invalidate the orbital analysis given in Chapters I* and II*.

d. Projections of the Domain of the Distribution

To apply these general conditions to two specific cases we choose again the typical points 1 and 2 on the (p,u^2)-plane. Figure 5-1 shows two sketches of projections of "safe orbits," orbits which have both tuning points (s_b, s_d) inside the diode, or in symbols, $s_a \geq s_b \geq s_d \geq 1$. The velocity coordinates have been normalized in terms of ω rather than kT_c:

$$X = 2\dot{r}/r_c\omega \quad , \quad Y = 2r\dot{\theta}/r_c\omega \quad . \tag{5.6}$$

On the left in each sketch the new-moon shaped curves represent extraordinary or cyclotron orbits, and on the right appear the ordinary or magnetron drift orbits. We met this distinction in (1.9*) and the sketch at the bottom of Fig.

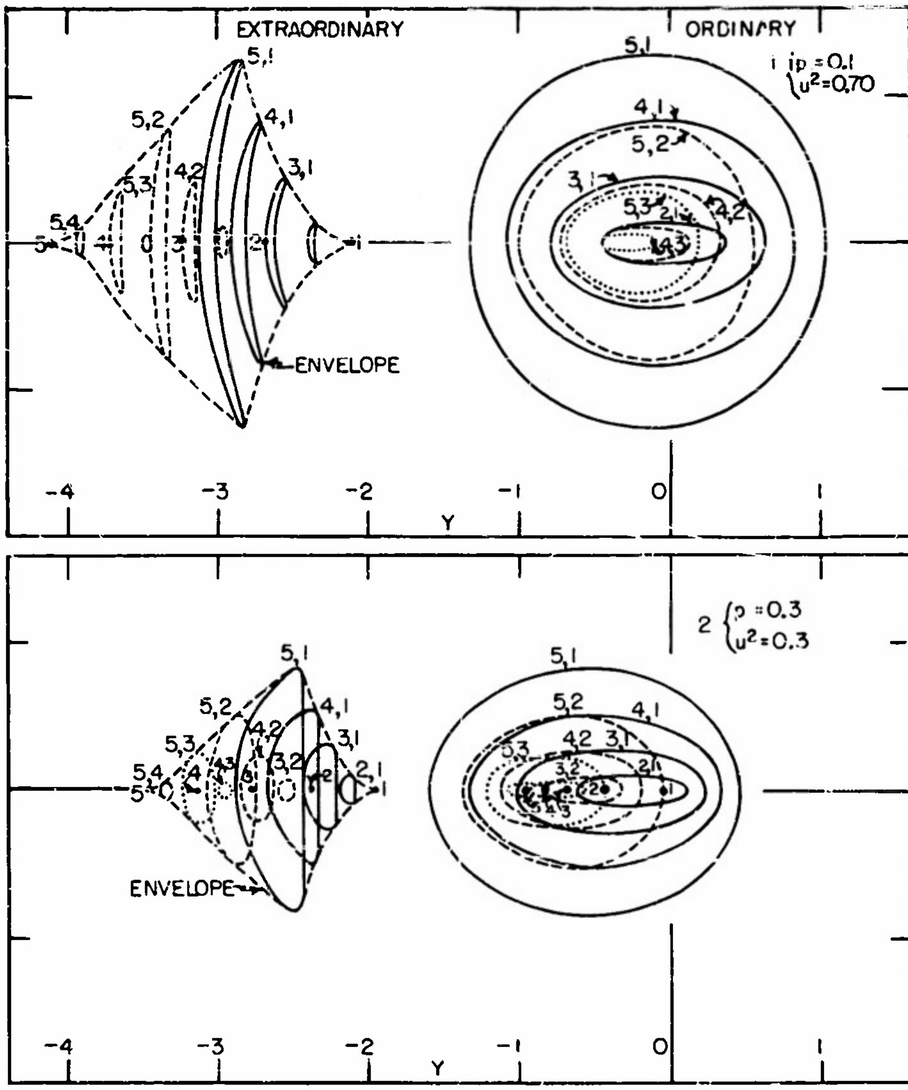

$X = 2\dot{r}/\omega r_c$, $Y = 2r\dot{\theta}/\omega r_c$, $p = -\frac{eV_a}{m\omega^2 r_c^2}$,

u = LAG COEFFICIENT

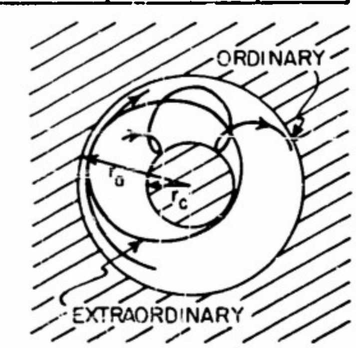

FIG 5-1 PROJECTIONS OF SAFE ORBITS (s_b, s_d) ON THE (XY) PLANE

5-1 may make it clearer. The cyclotron orbits, because they require high kinetic energies ($Y^2 > 4$), are presumably rarely occupied although they are as "safe" as the other type.

Figure 5-2 shows the projections of two sets of safe ordinary orbits on the subspace (Y,s). The sets are based on potential functions appropriate to the same two points on the (p,u^2)-plane. The individual projections are plotted from (1.6*) and (1.15*):

$$P = \sqrt{s}\,Y + s\ ;\quad u^2 s_g^{\,2} = P^2 + s_a\left(\frac{p}{p_c} - [1 - u^2]\right) - \frac{p}{p_c} \qquad (5.7)$$

P, we recall, is the normalized canonical momentum in the circumferential direction, and s_g is the mean radius of an orbit which has turning points (s_b, s_d). Eliminating P, we solve (5.7) for $Y(s)$, an expression in which the plus sign represents ordinary orbits:

$$Y(s) = -\sqrt{s} \pm \left\{\frac{s_a(1-u^2-p/p_c) + u^2 s_g^{\,2} + p/p_c}{s}\right\}^{1/2} \qquad (5.8)$$

Actually the dashed lines in Fig. 5-2 represent ten ordinary orbits, chosen as examples, with (s_b, s_d) from the group $s_b = 5,4,3,2,\ s_d = 4,3,2,1,\ s_b > s_d$. The boundaries of the projection of G on (Y,s) consist of the vertical lines $s = 1$, $s = s_a$, and the sloping solid curves. In each sketch, the upper curve forms the envelope of ends s_d of orbits which graze the anode, and the lower curve forms the envelope of turning points s_b of orbits which graze the cathode.

The dot-dash line in each sketch, $Y_g = Y(s_g)$, that cuts each orbit in half, is the locus of orbits of zero radial motion. One can define an effective potential U by reference to such orbits, orbits of minimum energy among all orbits having the same mean radius s_g. This potential is plotted in Fig. 5-3, and for comparison the potential $\chi(s)$ used in Chapter III. The radial dependence is given for the same typical cases, 1 and 2. Introducing the notation $(1 - u^2 - p/p_c) = \Delta \doteq 0$ for convenience, we have:

$$U \equiv Y_g^{\,2} - 8\Phi(s_g) = \left(\sqrt{(s_a-1)\Delta + 1 + u^2(s_g-1)} - 1\right)^2 - u^2(s_g-1)^2$$

$$\overline{\chi} \equiv s_g - 1 - 8\Phi(s_g) = (s_g - 1)\left[\left(\frac{s_a}{s_g} - 1\right)\Delta + 1 - \frac{p}{p_c}\left(\frac{s_g - 1}{s_g}\right)\right] \tag{5.9}$$

If $\underline{f}$ were plotted in a three-dimensional graph above the (Y,s)-plane, this graph probably would have a ridge or maximum above the dot-dash line Y_g. For if electrons are distributed in some statistical fashion according to their radial energies above the zero level given by U, this distribution must tend to pile up above Y_g. However, Y_g is also the locus of the points s_g of maximum radial motion in a given orbit, $X_g = X_m$. Charges in periodic motion spend more time near their turning points than near the orbit center and this tends to reduce the density above Y_g. Indeed, if Δn is the time-average contribution of a particle in an orbit (s_b, s_d) to the number density n in the interval Δs, then:

$$\Delta n = \frac{\omega u \Delta s}{\pi \dot{s}}, \quad \dot{s}^2 (s, s_g, j_r) \equiv s X^2 \omega^2 \tag{5.10}$$

Formulae (5.8) and (5.10) suggest that $\underline{f}$ can be expressed in terms of s_g and j_r, instead of X and Y. This cannot be carried out entirely while the form for the unbalanced radial transport current is unknown, but for the residual part of the distribution we suggest the following semi-Boltzmann form:

$$g_o(s_g) \frac{\exp\left\{-b(s_g)(j_r + j_z)\right\}}{\pi\sqrt{\frac{j_r s^*}{\pi} - (s^* - s_g)^2}} \, dj_r \, ds_g \, dj_z \, ds^* \tag{5.11}$$

Here $g_o(s_g)$ is partly a normalization factor. In the Boltzmann exponential, $b(s_g)$ represents a reciprocal temperature or characteristic energy and depends no doubt on T_c and V_a. In the same exponential term, $j_r = \pi X_m^2 / u^2$ (1.23*) is the radial action and j_z is a renormalization of $(\dot{z})^2$. The square root in the denominator represents $1/\dot{s}$. The variable s^* in it is to be integrated over the orbit interval between the limits:

$$s_b, s_d = s_g \left\{\sqrt{1 + \frac{j_r}{4\pi s_g}} \pm \sqrt{\frac{j_r}{4\pi s_g}}\right\}^2 . \tag{5.12}$$

Equations (4.16) and (5.11) provide a hypothesis which can be tested further in several ways. For instance, one might repeat the temperature

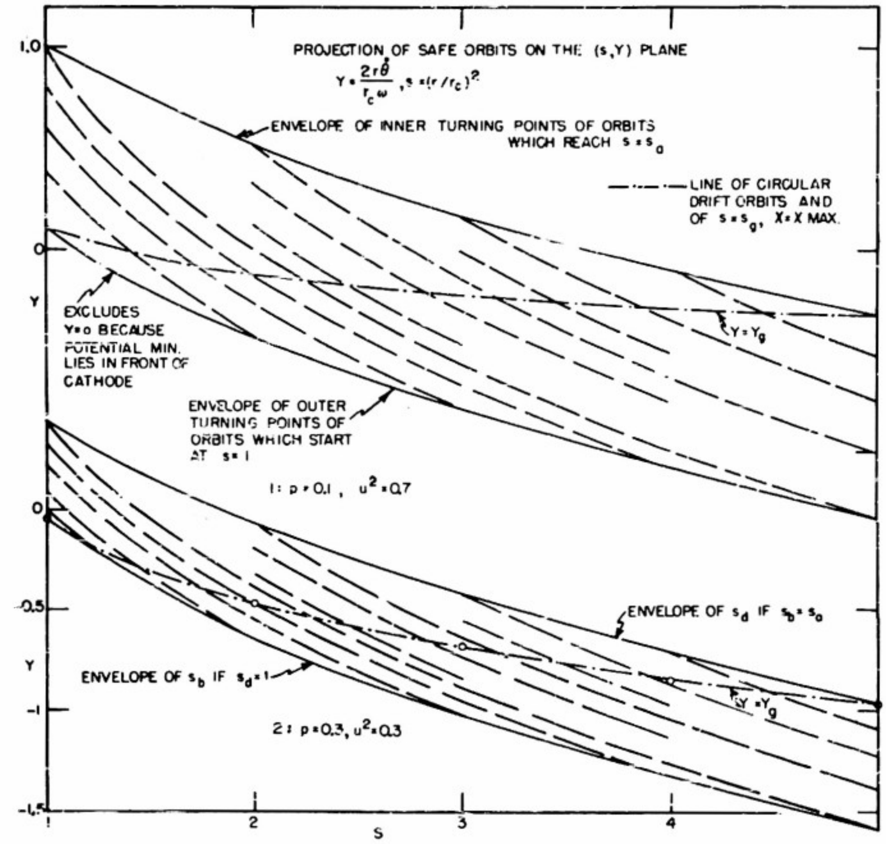

FIG. 5-2 PROJECTIONS OF SAFE ORBITS ON THE (s,Y) PLANE

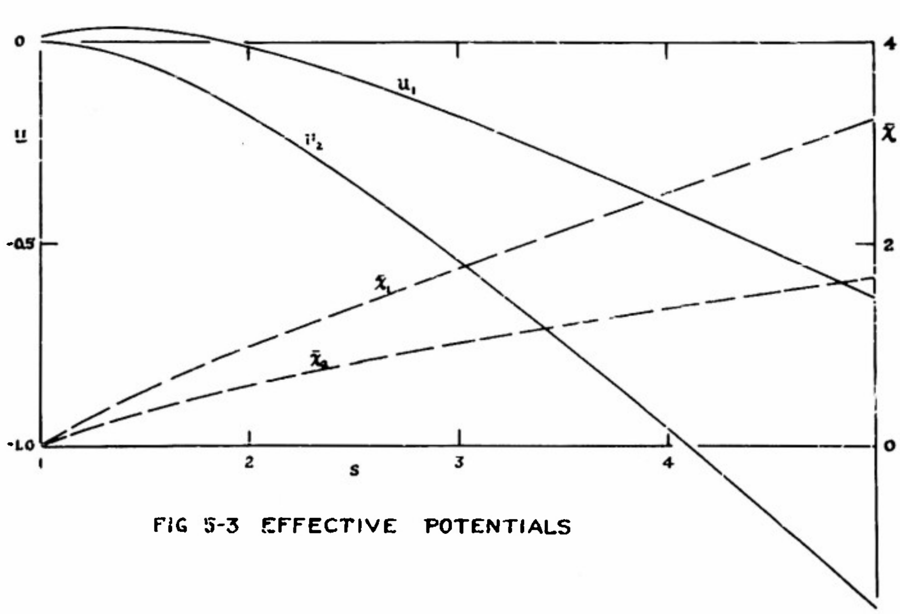

FIG 5-3 EFFECTIVE POTENTIALS

measurements (Linder and Wigdortschik) and electrostatic probe experiments (Engbert) mentioned in Chapter IV, and even Wasserman's [5] study of the magnetic field of the charge cloud, with refinements suggested by this analysis. The interference of the TEM probe signal with the transport process and the observed reduction in anode current at absorption resonance requires further study. Finally recent work in France on the space-charge amplification of noise in a linear magnetron ("diocotron") bears directly on the distribution of space charge after cutoff [6,7].

References in Chapter V

1. G. Hok, "A Statistical Approach to the Space-Charge Distribution in a Cutoff Magnetron," J. Appl. Phys. 23, 983-989, (1952).

2. Chapman and Cowling, The Mathematical Theory of Non-Uniform Gases, 2nd Edition, Cambridge University Press, Cambridge, 1952.

3. Debye and Hückel, "On the Theory of the Electrolyte," Phys. Z. (Leipzig), 24, 185-206 (1923).

4. Bohm and Pines, "A Collective Description of Electron Interactions," Phys. Rev. 82, 625-634 (1951); 85, 338-353, (1952); 92, 609-636 (1953).

5. I. Wassermann, "Space Charge in the Magnetron," J. Tech. Phys. U.S.S.R. 18, 785 (1948)(Zd. Tek. Fiz.)

6. Warnecke, Huber, Guenard, Doehler, "Amplification by Space-Charge Waves in a Beam in Crossed Electric and Magnetic Fields," C.R. Acad. Sci. (Paris) 235, 470 (1952), and many other recent papers.

7. G. D. Sims and P. A. Lindsay, "Application of Thermodynamics of Irreversible Processes to the Theory of the Magnetron," Proc. Phys. Soc. B 66, 423-5 (1953).

DISTRIBUTION LIST

Technical Reports

2	Chief of Naval Research (427) Department of the Navy Washington 25, D. C.
1	Chief of Naval Research(460) Department of the Navy Washington 25, D. C.
1	Chief of Naval Research (421) Department of the Navy Washington 25, D. C.
6	Director (Code 2000) Naval Research Laboratory Washington 25, D. C.
2	Commanding Officer Office of Naval Research Branch Office 150 Causeway Street Boston, Massachusetts
1	Commanding Officer Office of Naval Research Branch Office 1000 Geary Street San Francisco 9, California
1	Commanding Officer Office of Naval Research Branch Office 1030 E. Green Street Pasadena, California
1	Commanding Officer Office of Naval Research Branch Office The John Crerar Library Building 86 East Randolph Street Chicago 1, Illinois
1	Commanding Officer Office of Naval Research Branch Office 346 Broadway New York 13, New York
3	Officer-in-Charge Office of Naval Research Navy No. 100 Fleet Post Office New York, N. Y.

1	Chief, Bureau of Ordnance (Re4) Navy Department Washington 25, D. C.
1	Chief, Bureau of Ordnance (AD-3) Navy Department Washington 25, D. C.
1	Chief, Bureau of Aeronautics (EL-1) Navy Department Washington 25, D. C.
2	Chief, Bureau of Ships (810) Navy Department Washington 25, D. C.
1	Chief of Naval Operations (Op-413) Navy Department Washington 25, D. C.
1	Chief of Naval Operations (Op-20) Navy Department Washington 25, D. C.
1	Chief of Naval Operations (Op-32) Navy Department Washington 25, D. C.
1	Director Naval Ordnance Laboratory White Oak, Maryland
2	Commander U. S. Naval Electronics Laboratory San Diego, California
1	Commander (AAEL) Naval Air Development Center Johnsville, Pennsylvania
1	Librarian U. S. Naval Post Graduate School Monterey, California
50	Director Signal Corps Engineering Laboratories Evans Signal Laboratory Supply Receiving Section Building No. 42 Belmar, New Jersey

3	Commanding General (RDRRP) Air Research and Development Command Post Office Box 1395 Baltimore 3, Maryland
2	Commanding General (RDDDE) Air Research and Development Command Post Office Box 1395 Baltimore 3, Maryland
1	Commanding General (WCRR) Wright Air Development Center Wright-Patterson Air Force Base, Ohio
1	Commanding General (WCRRH) Wright Air Development Center Wright-Patterson Air Force Base, Ohio
1	Commanding General (WCRE) Wright Air Development Center Wright-Patterson Air Force Base, Ohio
2	Commanding General (WCRET) Wright Air Development Center Wright-Patterson Air Force Base, Ohio
1	Commanding General (WCREO) Wright Air Development Center Wright-Patterson Air Force Base, Ohio
2	Commanding General (WCLR) Wright Air Development Center Wright-Patterson Air Force Base, Ohio
1	Commanding General (WCLRR) Wright Air Development Center Wright-Patterson Air Force Base, Ohio
2	Technical Library Commanding General Wright Air Development Center Wright-Patterson Air Force Base, Ohio
1	Commanding General (RCREC-4C) Rome Air Development Center Griffiss Air Force Base Rome, New York
1	Commanding General (RCR) Rome Air Development Center Griffiss Air Force Base Rome, New York

2 Commanding General (RCRW)
Rome Air Development Center
Griffiss Air Force Base
Rome, New York

6 Commanding General (CRR)
Air Force Cambridge Research Center
230 Albany Street
Cambridge 39, Massachusetts

1 Commanding General
Technical Library
Air Force Cambridge Research Center
230 Albany Street
Cambridge 39, Massachusetts

2 Director
Air University Library
Maxwell Air Force Base, Alabama

1 Commander
Patrick Air Force Base
Cocoa, Florida

2 Chief, Western Division
Air Research and Development Command
P. O. Box 2035
Pasadena, California

1 Chief, European Office
Air Research and Development Command
Shell Building
60 Rue Ravenstein
Brussels, Belgium

1 U. S. Coast Guard (EEE)
1300 E Street, N. W.
Washington, D. C.

1 Assistant Secretary of Defense
(Research and Development)
Research and Development Board
Department of Defense
Washington 25, D. C.

5 Armed Services Technical Information Agency
Document Service Center
Knott Building
Dayton 2, Ohio

1 Director
Division 14, Librarian
National Bureau of Standards
Connecticut Avenue and Van Ness St., N. W.

1 Director
Division 14, Librarian
National Bureau of Standards
Connecticut Avenue and Van Ness St., N. W.

1 Office of Technical Services
Department of Commerce
Washington 25, D. C.

1 Commanding Officer and Director
U. S. Underwater Sound Laboratory
New London, Connecticut

1 Federal Telecommunications Laboratories, Inc.
Technical Library
500 Washington Avenue
Nutley, New Jersey

1 Librarian
Radio Corporation of America
RCA Laboratories
Princeton, New Jersey

1 Sperry Gyroscope Company
Engineering Librarian
Great Neck, L. I., New York

1 Watson Laboratories
Library
Red Bank, New Jersey

1 Professor E. Weber
Polytechnic Institute of Brooklyn
99 Livingston Street
Brooklyn 2, New York

1 University of California
Department of Electrical Engineering
Berkeley, California

1 Dr. E. T. Booth
Hudson Laboratories
145 Palisade Street
Dobbs Ferry, New York

1 Cornell University
Department of Electrical Engineering
Ithaca, New York

1 University of Illinois
Department of Electrical Engineering
Urbana, Illinois

1 Johns Hopkins University
Applied Physics Laboratory
Silver Spring, Maryland

1 Professor A. von Hippel
Massachusetts Institute of Technology
Research Laboratory for Insulation Research
Cambridge, Massachusetts

1 Director
Lincoln Laboratory
Massachusetts Institute of Technology
Cambridge 39, Massachusetts

1 Signal Corps Liaison Office
Massachusetts Institute of Technology
Cambridge 39, Massachusetts

1 Mr. Hewitt
Massachusetts Institute of Technology
Document Room
Research Laboratory of Electronics
Cambridge, Massachusetts

1 Stanford University
Electronics Research Laboratory
Stanford, California

1 Professor A. W. Straiton
University of Texas
Department of Electrical Engineering
Austin 12, Texas

1 Yale University
Department of Electrical Engineering
New Haven, Connecticut

1 Mr. James F. Trosch, Administrative Aide
Columbia Radiation Laboratory
Columbia University
538 West 120th Street
New York 27, N. Y.

1 Dr. J.V.N. Granger
Stanford Research Institute
Stanford, California